The interplay between small RNA pathways shapes chromatin landscape in *C. elegans*

E. Gushchanskaia[1], R. Esse[1], Q. Ma[1], N. Lau[1], A. Grishok[1*]

[1]Boston University School of Medicine, Biochemistry Department, Boston, 02118, USA

The nematode *C. elegans* contains numerous classes of endogenous small interfering RNAs (endo-siRNAs) produced by RNA-dependent RNA polymerase complexes (RdRP). Both “silencing” siRNAs bound by Worm-specific Argonautes (WAGO) and “activating” siRNAs bound by CSR-1 require the DRH-3 helicase, an RdRP component. Here we show that, in the *drh-3(ne4253)* mutant deficient in RdRP-produced secondary endo-siRNAs, the histone mark H3K27me3 ectopically accumulates at highly expressed genes. Moreover, we observe ectopic H3K9me3 at enhancer elements in both *drh-3* and *csr-1* partial loss-of-function mutants. Correlating with these chromatin changes in the mutants, there is a global increase in antisense transcription and a specific increase in enhancer RNA levels. Finally, we detect siRNA landscape changes in RdRP and *drh-3(ne4253)* mutants and accumulation of dsRNA in the nuclei of *drh-3(ne4253)* worms. Our study suggests that, in the absence of secondary siRNAs, elevated antisense transcription promotes nuclear dsRNA formation, which, in turn, can be cleaved by Dicer into primary siRNAs that guide deposition of silent chromatin marks.

Introduction

Research in fission yeast and plants identified an elaborate connection between siRNAs and heterochromatin formation (Pikaard and Mittelsten Scheid, 2014; Holoch and Moazed, 2015). To what extent this mechanism is conserved in other species is an important biological question. In the nematode *C. elegans,* as well as mammalian cultured cells, exogenous or transgene-based introduction of double-stranded RNA (dsRNA) can initiate transcriptional silencing and/or heterochromatin formation (Grishok et al., 2005; Gu et al., 2012; Burton et al., 2011; Gullerova and Proudfoot, 2012). Piwi-interacting RNAs (piRNAs) that protect the germline from parasitic elements are also strongly implicated in mechanisms triggering heterochromatin formation (Cecere and Grishok, 2014). Finally, there are endogenous siRNAs (endo-siRNAs) produced from the dsRNA segments arising from large hairpins, overlapping 5' or 3' ends of transcripts, or repetitive elements that have been detected in oocytes of higher animals (Watanabe et al., 2008; Tam et al., 2008). Whether endo-siRNAs also regulate heterochromatin is less clear. The detection of nuclear small RNA production at enhancers (Li et al., 2016) supports a regulatory potential of nuclear RNAi in animals.

In *C. elegans*, primary siRNAs generated through long dsRNA cleavage by the Dicer complex have been described in silencing induced by exogenous dsRNA (Yigit et al., 2006) or during viral infection (Sarkies et al., 2013). Consistently, the long dsRNA-binding protein RDE-4 (Tabara et al., 2002) and the primary siRNA-binding Argonaute RDE-1 (Yigit et al., 2006), which are required for these processes, are often referred to as antiviral RNAi pathway components. However, in the absence of the *C. elegans* ADARs (Double-Stranded RNA-Specific Adenosine Deaminases), there is ectopic

accumulation of nuclear dsRNA substrates for Dicer and ectopic activation of the antiviral RNAi pathway, which leads to developmental and physiological abnormalities (Tonkin, 2003; Warf et al., 2012; Reich et al., 2018). Most recently, Bass and colleagues described novel abundant endogenous siRNAs accumulating in the ADAR mutants that are likely responsible for these negative effects (Reich et al., 2018).

In wild type *C. elegans*, the most abundant endo-siRNAs are 22G-RNAs produced by RNA-dependent RNA Polymerases (RdRP). In the antiviral pathway, primary siRNAs bound by RDE-1 are ultimately responsible for the recruitment of RdRPs to the 3' uridylated mRNA fragments and amplification of the RNAi response through secondary 22G-RNAs (Tsai et al., 2015). In the endogenous RNAi pathways, either ERGO-1-bound primary siRNAs or piRNAs initiate 22G-RNA production (Yigit et al., 2006; Han et al., 2009; Vasale et al., 2010; Ashe et al., 2012; Buckley et al., 2012; Gu et al., 2012; Luteijn et al., 2012; Shirayama et al., 2012). These pathways target repetitive elements, pseudogenes, transposons, and some duplicated protein-coding genes for silencing. A group of redundant Worm-specific AGO proteins (WAGO) bind 22G-RNAs generated downstream of both antiviral and endogenous RNAi silencing pathways. The nuclear WAGOs implicated in inducing transcriptional silencing are NRDE-3, expressed in the soma, and HRDE-1, expressed in the germline. There is evidence that these proteins are capable of inducing H3K9me3 at endogenous genes complementary to exogenous dsRNA or at transgenes downstream of piRNAs (Guang et al., 2008; Guang et al., 2010; Burton et al., 2011; Ashe et al., 2012; Buckley et al., 2012; Gu et al., 2012; Luteijn et al., 2012; Shirayama et al., 2012). At endogenous WAGO targets, i.e. repetitive elements, pseudogenes, and transposons, the connection between 22G-RNA production, H3K9

methylation and transcriptional silencing has not been extensively examined (Moazed et al., 2006; Burkhart et al., 2011; Ni et al., 2014). In addition, the possibility of H3K27 methylation guided by 22G-RNAs has not been tested.

Whereas the concept that nuclear Argonaute proteins guide silencing histone modifications is well established, the CSR-1 (Chromosome Segregation and RNAi deficient) Argonaute (Yigit et al., 2006; Claycomb et al., 2009) does not fit this stereotype. It is present both in the cytoplasm and the nucleus, it binds 22G-RNAs that are largely antisense to highly and widely expressed genes, and it is associated with the nascent transcripts and mature mRNAs complementary to these siRNAs. In contrast to direct gene-silencing roles for WAGOs, CSR-1 has an “activating” or “anti-silencing” role, since the levels of nascent transcripts complimentary to CSR-1-bound siRNAs decrease in *csr-1*-deficient worms (Cecere et al., 2014). Earlier, we took a genomic approach for studying CSR-1 function (Global Ran-on Sequencing or GRO-seq) and detected both a decrease in nascent transcripts targeted by CSR-1 siRNAs and a remarkable increase in antisense transcription genome-wide in *csr-1* and *drh-3* partial loss-of-function mutants (Cecere et al., 2014). Notably, DRH-3 (Dicer-related helicase) is a component of RdRP complexes producing 22G-RNAs and is required for generation of both WAGO-bound and CSR-1-bound small RNAs.

Here, we report a re-distribution of H3K27 methylation from the repetitive elements and X chromosome to active genes (CSR-1 targets) in *drh-3(ne4253)* mutant worms, correlating with an increase in antisense transcription at these loci. Moreover, we show that in both *csr-1* and *drh-3* mutants there is an increase in enhancer RNA transcription and elevation in H3K9me3 at enhancers. Finally, we identify small RNAs originating from

enhancers in previously published datasets, including CSR-1 IP samples. Our results support a model whereby "activating" and "silencing" secondary siRNAs in *C. elegans* have complementary functions required for proper genome-wide chromatin organization. We propose that in the absence of secondary siRNAs, there is excessive dsRNA production and activation of the antiviral RNAi pathway, which has the potential in driving ectopic methylation of both H3K9 and H3K27.

Results

Histone H3K27 methylation is ectopically increased on highly active genes upon drh-3 loss-of-function

Previously, we observed similar alterations in global transcription in the viable partial loss-of-function *csr-1* and *drh-3* mutant larvae compared with wild type animals (Cecere et al., 2014). To establish a connection between transcription changes and chromatin status in these mutants, we performed ChIP-seq with antibodies specific to several histone modifications: H3K27me3, H3K36me3, and H3K9me3.

The data obtained using wild type worms are consistent with the previous studies (Schmitges et al., 2011; Yuan et al., 2011; Gaydos et al., 2014) and demonstrate that H3K36me3 is linked to actively transcribed genes, while H3K27me3 is enriched in regions with low transcription activity (Fig. 1A).

In *drh-3(ne4253)*, transcription reduction of normally highly expressed genes strongly correlates with a reduction in the levels of active histone modification H3K36me3 and a gain of repressive histone mark H3K27me3 (Fig. 1B). The highly expressed messages are known to be complementary to CSR-1-bound small RNAs (i.e. they represent CSR-1 target genes) (Claycomb et al., 2009). Therefore, a global reduction in H3K36me3 accompanied by a gain in H3K27me3 occurs at these CSR-1 target genes in *drh-3(ne4253)* (Fig. 1C, left panel and Fig. 1D).

At the same time, we observed that transcriptionally silent regions (pseudogenes and tissue-specific genes) that become more active in *drh-3(ne4253)* gain H3K36me3 and lose H3K27me3 in the *drh-3(ne4253)* mutant (Supplemental Fig. 1).

Surprisingly, in the partially rescued *csr-1(tm892)* mutant (strain WM193, (Claycomb et al., 2009)), we did not observe dramatic changes in chromatin modifications (Fig. 1C, right panel), even though transcription changes similar to those occurring in *drh-3(ne4253)* take place in this mutant as well (Cecere et al., 2014). It is possible that a loss of CSR-1-interacting siRNAs in *drh-3(ne4253)* causes a more severe effect on the CSR-1/siRNA complex function than a decrease in CSR-1 protein level in the partially rescued *csr-1(tm892)* mutant (Cecere et al., 2014). Alternatively, the distinct molecular phenotypes, that is: the partial loss of only the “activating” pathway in the *csr-1* mutant and the perturbation of both “activating” and “silencing” pathways in the *drh-3* mutant can result in different changes in chromatin.

Overall, our results indicate that a loss of both “activating” and “silencing” siRNAs results in dramatic redistribution of H3K36me3 and H3K27me3 histone modifications along gene bodies. Since WAGO siRNAs are absent in the *drh-3(ne4253)* mutant, we

conclude that there must be additional mechanisms responsible for the deposition of ectopic H3K27me3 observed at the CSR-1 target genes.

Opposite regulation of H3K9me3 on highly active genes by the CSR-1 and WAGO pathways

Since the WAGO pathway is implicated in regulating H3K9me3, a mark associated with silent heterochromatin (Guang et al., 2008; Guang et al., 2010; Burton et al., 2011; Ashe et al., 2012; Buckley et al., 2012; Gu et al., 2012; Luteijn et al., 2012; Shirayama et al., 2012), we examined H3K9me3 by ChIP-seq next. Consistent with the published data (Liu et al., 2011), H3K9me3 was found predominantly at the chromosome arms (Fig. 2A). Whereas the level of H3K9me3 increases at the CSR-1 target genes in the *csr-1* mutant compared to wild type (Fig. 2B, left plot), in *drh-3(ne4253)* we observed a depletion of this silencing mark at the same genes (Fig. 2B, right plot). Because both the CSR-1 and the WAGO pathways are deficient in the *drh-3(ne4253)* mutation background, these results suggest a competition between the “activating” and “silencing” secondary siRNAs, such that the WAGO pathway promotes H3K9me3 and CSR-1 inhibits its deposition at the majority of CSR-1 target genes. This type of competitive relationship has been suggested by other studies utilizing transgenic strains (Ashe et al., 2012; Lee et al., 2012; Shirayama et al., 2012).

Our results are consistent with the idea that ectopic H3K27me3 is associated with a reduction in expression of highly active genes in *drh-3(ne4253)*, whereas in the *csr-1* mutant, the WAGO-induced H3K9me3 is likely to play a more prominent role in inhibiting

active genes. Therefore, CSR-1-bound siRNAs protect highly expressed genes from both WAGO-dependent H3K9me3 deposition and H3K27me3 deposition driven by additional mechanisms.

Increase in antisense RNA production upon csr-1 and drh-3 loss-of-function correlates with accumulation of silencing marks

Another striking observation was made while analyzing heterochromatic histone modifications at enhancer regions in the studied loss-of-function mutants. Notably, in both *csr-1* and *drh-3* mutants, H3K9me3 is increased at the enhancer regions defined by a recent ATAC-seq study (Daugherty et al., 2017) (Fig. 2C). Therefore, it is possible that RdRP-produced small RNAs promote enhancer function by antagonizing, directly or indirectly, chromatin compaction at these regions.

Previously, we described a global increase in antisense transcription in the *csr-1* and *drh-3* mutant larvae (Cecere et al., 2014). To determine whether regions showing ectopic silencing marks in these mutants produce antisense RNA, we re-analyzed our published GRO-seq data. Indeed, we detected an increase in antisense transcription at CSR-1 target genes in both mutants (Fig. 3A, CSR-1 targets). Interestingly, the increase was most prominent at the genes containing enhancers regardless of their CSR-1 target/non-target status (Fig. 3A, genes with enhancers).

To further analyze transcription associated with the potential enhancer regions, we used enhancer-mapping data from two recent publications (Evans et al., 2016; Daugherty et al., 2017). The first study (Evans et al., 2016) predicted enhancer locations using

established chromatin signatures and was beneficial for our analysis, having been performed on the same larval stage (L3) that was used in our GRO-seq (Cecere et al., 2014) and ChIP-seq experiments. In another study (Daugherty et al., 2017), open chromatin regions associated with enhancers were detected by ATAC-seq and the functionality of some was confirmed. Our analysis of GRO-seq data identified a global increase in transcription at putative enhancers in both *csr-1* and *drh-3* mutants (Fig. 3B). We confirmed this result using the ATAC-seq-based enhancer mapping dataset for distal (intergenic) enhancers (Fig. 3C). As an example of increased transcription at a potential enhancer we demonstrate the *daf-12* gene upstream regulatory region that was shown to be L3 stage-specific in previous studies (Antebi et al., 1998; Daugherty et al., 2017) (Fig. 3D).

In summary, we observed an increase in antisense transcription at CSR-1 target genes and an increase in enhancer RNA transcription in the absence of RdRP-produced small RNAs. These results suggest that dsRNA accumulates at these regions in *drh-3* and *csr-1* mutants, thereby ectopically triggering dsRNA-dependent antiviral RNAi pathway that elevates silencing chromatin marks. Consistent with this possibility, the importance of cis-dsRNA synthesis for siRNA-induced chromatin silencing (Iida et al., 2008), as well as a correlation between increased convergent transcription and heterochromatin formation (Gullerova and Proudfoot, 2012), was reported previously in fission yeast.

dsRNA-derived primary small RNA may induce histone modifications in the absence of secondary siRNAs

Since the majority of worm small antisense RNAs are represented by secondary siRNAs (22G-RNAs) produced by RdRPs, we examined how significantly the siRNAs were depleted in the RdRP complex mutants. Two *C. elegans* RdRPs: EGO-1 and RRF-1 have partially overlapping functions in secondary siRNA generation (Gu et al., 2009). By quantifying existing datasets of small RNAs cloned from the RdRP and other RNAi-related mutants (Gu et al., 2009; Claycomb et al., 2009), we interrogated whether primary siRNAs produced by Dicer cleavage might increase so as to compensate for the absence of RdRP-generated secondary, and mostly antisense, siRNAs. We compared the proportion of small antisense RNAs targeting gene targets in the wild type and the RdRP complex mutants: *drh-3(ne4253), ego-1(om97),* and *ego-1; rrf-1* (Gu et al., 2009). As expected, antisense RNAs comprises 90-95% of the total pool in wild type. In the RdRP mutants, the proportion of antisense RNAs drops to 50-35% (Fig. 4A), consistent with the equal representation of sense and antisense RNAs in the siRNA duplex generated by Dicer.

To specifically examine the changes in the siRNA landscape at the CSR-1 target genes, we chose a cluster of histone genes on chromosome four (Fig. 4B). In wild type worms, small RNAs mapping to this region largely correspond to antisense 22G-RNAs binding to CSR-1 (Fig. 4B, CSR-1 IP track). Strikingly, in the *drh-3(ne4253)* worms, there are more sense than antisense RNAs at this locus, and in the RdRP mutants the

symmetric signature of both sense and antisense small RNAs matching each gene is apparent.

To validate the idea of dsRNA accumulation in *drh-3* and *csr-1* mutants, we performed immunostaining of intestinal cells with an antibody recognizing long dsRNA (J2, (Stollar and Stollar, 1970; Bonin et al., 2000)). In the *csr-1* mutant, the dsRNA accumulation is not extensive, but in *drh-3(ne4253)* we observed a strong staining signal in the nucleus (Fig. 4C). We confirmed the specificity of the antibody by using RNase A-treated control samples (Supplemental Fig. 2).

Finally, we sought small RNAs originating from enhancers in the published datasets (Gu et al., 2009; Claycomb et al., 2009), (Fig. 4D, Supplemental Fig. 3). Indeed, about 6-7% of small RNA reads map to the enhancer domains defined by the Ahringer group (Evans et al., 2016). Moreover, they are present in the CSR-1 IP samples and notably increase in abundance, to 9-11%, in the RdRP complex mutants (Fig. 4D, Supplemental Fig. 3). Therefore, an increase in enhancer small RNAs detected upon *drh-3* loss-of-function correlates with elevation of H3K9me3 at enhancers in this mutant background.

Discussion

The nuclear accumulation of dsRNA in *drh-3(ne4253)* and the appearance of the primary siRNA signature in the population of small RNAs present in RdRP mutants strongly suggest that the antiviral RNAi pathway is ectopically activated in the absence of secondary small RNAs. Moreover, the ectopic H3K27me3 at the CSR-1 target genes and

H3K9me3 at the enhancers observed in *drh-3(ne4253)* is likely guided by this new population of Dicer-dependent small RNAs. We propose a revised model whereby CSR-1-bound antisense RNAs protect their RNA targets both from the WAGO-induced and antiviral RNAi pathway-induced silencing in the nucleus (Fig. 5).

Our results suggest the exciting possibility that secondary siRNAs bound by CSR-1 may directly limit enhancer RNA transcription, therefore antagonizing the production of long dsRNA and heterochromatin formation at these regulatory regions. It is possible that CSR-1 promotes 3'-end processing of enhancer RNA, similarly to its effect on histone pre-mRNA (Avgousti et al., 2012). The difference between these two types of RNA and the majority of protein-coding pre-mRNAs targeted by antisense CSR-1-bound siRNAs is the presence of introns in the latter case. Perhaps interaction with the splicing components, such as helicase EMB-4/Aquarius (Tyc et al., 2017), does not allow CSR-1 to cleave the majority of its targets in the nucleus. Instead, both CSR-1 and splicing factors may prevent the interaction of pre-mRNAs with the complementary antisense or piRNA species.

Nuclear RNAi in *C. elegans* has been mainly associated with secondary small RNAs generated in the cytoplasm that then move to the nucleus to execute their function (Guang et al., 2008; Guang et al., 2010; Burkhart et al., 2011; Burton et al., 2011; Ashe et al., 2012; Buckley et al., 2012; Gu, S.G., et al. 2012; Luteijn et al., 2012; Shirayama et al., 2012). They are considered to be functionally equivalent to the nuclear dsRNA-derived Dicer products in fission yeast, a mechanistically well-studied system of RNAi-induced transcriptional silencing and heterochromatin formation (Holoch and Moazed, 2015). However, other reports, most notably those describing a competition between

nuclear ADARs and the antiviral RNAi pathway components targeting dsRNA, strongly suggest that another Dicer-dependent RNAi process initiates in the nucleus (Warf et al., 2012; Reich et al., 2018; Tonkin, 2003). Consistently, phosphorylation-regulated nuclear localization of Dicer has been observed in *C. elegans* and mammalian cells (Drake et al., 2014).

Here, we uncover a surprising role of the *C. elegans* secondary siRNA system in inhibiting dsRNA production in the nucleus to prevent ectopic heterochromatin deposition. We propose that siRNAs produced by Dicer cleavage guide this process. This new silencing pathway can be more readily related to organisms lacking RdRPs, such as *Drosophila* and mammals.

Our work links deregulation of the nuclear 22G-RNA pathways to ectopic H3K9 and H3K27 methylation. Both histone marks can be artificially induced on active genes targeted by exogenous dsRNA (Guang et al., 2010; Mao et al., 2015). However, it was not possible to reliably correlate NRDE-3 or HRDE-1 function in regulation of endogenous genes with these silencing modification marks (Gu et al., 2012). Notably, in our experiments, dramatic chromatin rearrangements are only observed in the *drh-3(ne4253)* mutant background, when both CSR-1 and WAGO pathways are inactive. Our results suggest that, in *drh-3(ne4253),* loss of CSR-1 binding to its target pre-mRNAs may now allow antisense RNAs to accumulate and hybridize with these pre-mRNAs to produce dsRNAs as Dicer substrates for ectopic siRNAs. This may then lead to histone methyltransferase (HMT) complexes normally working with WAGO to now become ectopically distributed into the freed “CSR-1 territory”. Thus, ectopic siRNAs and HMTs

may finally induce chromatin changes. Ectopic deposition of H3K27me3 at CSR-1 targets in *drh-3(ne4253)* may occur through such a mechanism.

At the tissue-specific spermatogenesis genes, a loss of H3K27me3 takes place in *drh-3(ne4253).* This is accompanied by ectopic expression of these genes in *drh-3(ne4253)* L2 larvae (Supplemental Fig. 3). However, we have not observed this increased expression in either *nrde-3(gg64)* or *hrde-1(tm1200)* mutant worms (Supplemental Fig. 3). Both NRDE-3 and HRDE-1, in complex with 22G-RNAs, strongly interact with their target pre-mRNAs (Guang et al., 2008; Ashe et al., 2012; Buckley et al., 2012; Shirayama et al., 2012). It is possible that when NRDE-3 or HRDE-1 are missing, their target pre-mRNAs may also engage with antisense RNAs and form dsRNA. In this case, the dsRNA-induced silencing will substitute for the silencing role of WAGOs. The absence of both CSR-1-bound siRNAs and WAGO-bound siRNAs may create further competition for HMTs and lead to reduction of H3K27me3 at tissue-specific genes.

We have also detected a competition between the CSR-1 and WAGO pathways: CSR-1 appears to protect its targets from deposition of H3K9me3, likely guided by WAGO. This result is consistent with published work (Seth et al., 2013; Wedeles et al., 2013; Shen et al., 2018).

Notably, the re-distribution of H3K27me3 to active autosomal genes (i.e. CSR-1 targets) also occurs in the absence of H3K36 methylation at these genes in the germline of *mes-4* mutant worms (Gaydos et al., 2012). The H3K36 methyltransferase in yeast has been implicated in suppressing antisense transcription (Venkatesh et al., 2016), and it is possible that, in *C. elegans* and other animals, it prevents dsRNA formation and ectopic silencing of active genes.

Importantly, an independent line of research from our lab identified a role for H3K79 methylation in suppressing dsRNA formation and RNAi-induced H3K9me2 deposition at the enhancers (Esse et al., 2018). Therefore, studies in *C. elegans* revealed multiple mechanisms that have evolved to suppress inappropriate nuclear RNAi. Some of them, such as ADAR action (Warf et al., 2012), H3K79 methylation (Esse et al., 2018), and possibly H3K36 methylation, are likely conserved. Although the nuclear dsRNA inhibition via the secondary siRNA system that we describe here is unique to nematodes, other protein complexes interacting with pre-mRNAs, such as splicing factors, may have this additional role in higher organisms.

Materials and methods

Strains

Strains were maintained at 20 °C unless otherwise noted, using standard methods (Brenner, 1974). Bristol N2 was the WT strain used. Mutants used in this study were *drh-3(ne4253),* partially rescued *csr-1(tm892*) (strain WM193), *nrde-3(gg64)* and *hrde-1(tm1200)*. For the ChIP-seq experiments, worm populations were synchronized and grown for approximately 40 h after hatching at 20 °C on OP-50 *E. coli* at a density of ~50,000 animals per 15-cm Petri dish until they reached L3 stage. For steady-state expression analysis, worm populations were grown 5-7 h after synchronization.

ChIP

Chromatin immunoprecipitation was performed following the modENCODE Protocol from the Lieb Lab (modENCODE Consortium et al., 2009) with some modifications. The worm pellet fixed with 2% PFA for 30 minutes at 20°C was washed in M9 3 times and resuspended in RIPA buffer supplemented with Protease inhibitors (Thermo Scientific, 78443). DNA fragmentation was performed using sonication with Covaris (Peak power 240, Duty factor 20, Cycles/burst 200, 8 min). Then, 1.5–2mg of cross-linked chromatin extract was incubated at 4°C ON with a specific antibody and the immune complexes were then incubated with 50 µl IgG Dynabeads (Invitrogen) for 3h at 4°C. DNA was cleaned up with the Qiagen PCR purification kit. We used the following antibodies: 5 µg of anti-H3K27me3 (Diagenode, pAb-195-050), 5 µg of anti-H3K36me3 (Abcam, ab9050), 5 µg of anti-H3K9me3 (Abcam, ab8898). Validation information for the commercial antibodies is included at the manufacturers' websites.

Library preparation, sequencing and data processing

ChIP-seq libraries were prepared using TruSeq Illumina kit (set A – 15034288, set B - 15034289) according to manufacturer's instructions. Sequencing was performed on Illumina NextSeq500. The 75-bp single-end Illumina sequencing reads were preprocessed by trimming the adapter sequences with Cutadapt (Didion et al., 2017). After that, reads were aligned to the WS220/ce10 assembly of the *C. elegans* genome using Bowtie for Illumina (Galaxy Version 1.1.2) (Langmead et al., 2009) with default settings. The SAMtools (Galaxy Version 1.1.2) (Li et al., 2009; Li, 2011) utility was used

to convert the alignments to BAM format. A table containing the number of reads aligned to genome is included in supplementary data (Supplemental Table 1).

Two independent ChIP experiments were performed with each type of antibody. Comparison of the results demonstrated good reproducibility of the data (Supplemental Table 2). Duplicates reads were removed, and the data were processed as described below.

Analysis of GRO-seq data

GRO-seq reads (Cecere et al., 2014) were aligned to the WS220/ce10 assembly of the *C. elegans* genome using Bowtie for Illumina (Galaxy Version 1.1.2) (Langmead et al., 2009) with default settings. Reads matching ribosomal RNA loci were removed, as described before (Cecere et al., 2013). Read counting at specific loci (either genes, annotated regions or genomic bins) was performed with package GenomicAlignments (Lawrence et al., 2013); only reads with mapping quality 20 or higher were included in subsequent analyses. Regions without reads across the sample set were removed. Counts were then normalized using the TMM method, which takes RNA composition bias into account (Robinson and Oshlack, 2010), using the edgeR package (Robinson et al., 2010). Coverage was expressed as RPKM (reads per kilobase per million mapped) and log2-transformed.

Analysis of ChIP-seq data

Analysis of ChIP-seq data was performed as described for the analysis of GRO-seq data, with the exception that, after normalization of read counts, coverage was expressed as the log2-transformed ratio of the RPKM value in the immunoprecipitated DNA sample divided by the RPKM value in the non-immunoprecipitated (input) DNA. Only regions in which the normalized count value in the immunoprecipitated DNA sample was higher than that in the corresponding input DNA in at least one sample in the set were considered.

Analysis of chromatin domains and ATAC-seq peaks

Coordinates of chromatin domains were obtained from Evans et al., 2016. Putative enhancer regions were obtained by combining coordinates of domains 8, 9 and 10. Enhancer domains at least 1500 bp distal to any annotated transcription start site or transcription termination site were considered distal enhancer domains. Enhancer domains intersecting coordinates of genes < 15kb by at least 50 bp were considered intragenic enhancer domains. ATAC-seq peak coordinates (Daugherty et al., 2017) were downloaded from the NCBI GEO database (GSE89608). Distal and intragenic ATAC-seq peaks were obtained as for enhancer domains. CSR-1 target genes were obtained from (Claycomb et al., 2009). Gene identifiers were converted to Refseq mRNA IDs using the WormBase Converter utility (http://wormbasemanager.sourceforge.net/) and the DAVID Gene ID Conversion Tool (Huang et al., 2008). Intersections of genomic intervals were performed in R using the valr package (Riemondy et al., 2017).

Small RNA bioinformatics analyses

Small RNA library sequences were downloaded from the NCBI Gene Expression Omnibus and Sequence Read Archive under the following accessions: GSM454002, GSM455389, GSM455390, GSM455387, GSM455388, SRR030720, SRR030721, SRR030722, SRR030719, and SRR030717. Fastq files were validated and adapters were trimmed with the programs Fastqc (Brown et al., 2017) and Cutadapt (Didion et al., 2017), respectively. The genome and Refseq transcript assemblies for "ce10" were loaded into our custom "gene-centric process" small RNA analyses pipeline (Sytnikova et al., 2014; Chirn et al., 2015). This program maps small RNAs with Bowtie1 (Langmead et al., 2009) with a maximum of 2 base mismatches, counts the genomic strand reads against the Ensembl gene transcript models using Bedtools (Quinlan, 2014) using the longest transcript isoform as the main gene model, and generates WIG plots for coverage visualization on the UCSC Genome Browser (Speir et al., 2016). Each library's read counts were normalized against library depths (counts per million, cpm), as well as frequency of genomic locations (cpm / number of genomic loci).

For further analysis small RNA read coordinates were intersected with enhancer domain coordinates (Evans et al., 2016). For graphical representation purposes, the total number of reads for each sample was reduced to the number of reads observed in the sample with minimal read coverage (i.e. down sampling was performed). Percentages of reads were obtained and grouped in blocks with each block representing 1500 reads.

Immunostaining

Young adult worms were handpicked and placed in M9 solution supplemented with 0.01% Tween and 25mM sodium azide on a slide. Worms were dissected using scalpel and fixed with 2% PFA for one hour at room temperature and post-fixed in ice-cold methanol for 5 minutes. Control worms were treated with RNase A prior to fixation at 37°C for 30 minutes to confirm the antibody specificity and then washed 3 times with M9. After fixation, worms were transferred to glass tubes and blocked with 1% BSA in M9 supplemented with 0.05% Tween-20. Blocked samples were then incubated with the J2 antibody (a generous gift from Dr. Mühlberger; National Emerging Infectious Diseases Laboratories, Boston) (1:1000) overnight at 4°C, washed 3 times in washing buffer (BSA 0.25%, Tween-20 0.05% in M9), and then incubated with secondary fluorophore-conjugated (AF 568) antibody (1:500) for two hours in the dark room. After 3 washes, the samples were transferred to a slide and mounted with DAPI-containing solution (Invitrogen, Prolong Diamond Antifade Mountant with DAPI). The images were taken at 63x on a Zeiss AxioImager Z1 instrument and processed with ImageJ (version 1.51k).

Author contributions

E.G. conducted experiments and analyzed data, R.E. analyzed data, Q.M. and N.L. analyzed small RNA data, A.G. supervised the project. E.G. and A.G. wrote the manuscript.

Acknowledgements

We are grateful to the Mello and Kennedy labs for providing RNAi mutant strains. Some strains used in this study were obtained from the *Caenorhabditis Genetics Center*, which is funded by NIH Office of Research Infrastructure Programs (P40 OD010440). We thank Dr. Cifuentes' lab for fruitful discussions and Dr. Ritter for advising us on microscopy techniques. We thank the BU Microarray and Sequencing Resource Core Facility (CTSA grant UL1-TR001430) for sequencing the ChIP-seq libraries. We are thankful to Yunfan (Frank) Liang for help with qPCR and immunostaining experiments. This research was supported by the NIH R01 GM107056 award to AG.

References

Akay, A., Di Domenico, T., Suen, K.M., Nabih, A., Parada, G.E., Larance, M., Medhi, R., Berkyurek, A.C., Zhang, X., Wedeles, C.J., et al. (2017). The Helicase Aquarius/EMB-4 Is Required to Overcome Intronic Barriers to Allow Nuclear RNAi Pathways to Heritably Silence Transcription. Developmental Cell *42*, 241-255.e6.

Antebi, A., Culotti, J.G., and Hedgecock, E.M. (1998). daf-12 regulates developmental age and the dauer alternative in Caenorhabditis elegans. Development *125*, 1191–1205.

Ashe, A., Sapetschnig, A., Weick, E.-M., Mitchell, J., Bagijn, M.P., Cording, A.C., Doebley, A.-L., Goldstein, L.D., Lehrbach, N.J., Le Pen, J., et al. (2012). piRNAs Can Trigger a Multigenerational Epigenetic Memory in the Germline of C. elegans. Cell *150*, 88–99.

Avgousti, D.C., Palani, S., Sherman, Y., and Grishok, A. (2012). CSR-1 RNAi pathway positively regulates histone expression in *C. elegans*: RNAi in *C. elegans* regulates histone expression. The EMBO Journal *31*, 3821–3832.

Bonin, M., Oberstraß, J., Lukacs, N., Ewert, K., Oesterschulze, E., Kassing, R., and Nellen, W. (2000). Determination of preferential binding sites for anti-dsRNA antibodies on double-stranded RNA by scanning force microscopy. RNA *6*, 563–570.

Brenner, S. (1974). The genetics of Caenorhabditis elegans. Genetics *77*, 71–94.

Brown, J., Pirrung, M., and McCue, L.A. (2017). FQC Dashboard: integrates FastQC results into a web-based, interactive, and extensible FASTQ quality control tool. Bioinformatics.

Buckley, B.A., Burkhart, K.B., Gu, S.G., Spracklin, G., Kershner, A., Fritz, H., Kimble, J., Fire, A., and Kennedy, S. (2012). A nuclear Argonaute promotes multigenerational epigenetic inheritance and germline immortality. Nature *489*, 447–451.

Burkhart, K.B., Guang, S., Buckley, B.A., Wong, L., Bochner, A.F., and Kennedy, S. (2011). A Pre-mRNA–Associating Factor Links Endogenous siRNAs to Chromatin Regulation. PLoS Genetics *7*, e1002249.

Burton, N.O., Burkhart, K.B., and Kennedy, S. (2011). Nuclear RNAi maintains heritable gene silencing in Caenorhabditis elegans. Proceedings of the National Academy of Sciences *108*, 19683–19688.

Cecere, G., and Grishok, A. (2014). A nuclear perspective on RNAi pathways in metazoans. Biochimica et Biophysica Acta (BBA) - Gene Regulatory Mechanisms *1839*, 223–233.

Cecere, G., Hoersch, S., Jensen, M.B., Dixit, S., and Grishok, A. (2013). The ZFP-1(AF10)/DOT-1 Complex Opposes H2B Ubiquitination to Reduce Pol II Transcription. Molecular Cell *50*, 894–907.

Cecere, G., Hoersch, S., O'Keeffe, S., Sachidanandam, R., and Grishok, A. (2014). Global effects of the CSR-1 RNA interference pathway on the transcriptional landscape. Nature Structural & Molecular Biology *21*, 358–365.

Chekanova, J.A., Gregory, B.D., Reverdatto, S.V., Chen, H., Kumar, R., Hooker, T., Yazaki, J., Li, P., Skiba, N., Peng, Q., et al. (2007). Genome-Wide High-Resolution Mapping of Exosome Substrates Reveals Hidden Features in the Arabidopsis Transcriptome. Cell *131*, 1340–1353.

Chirn, G.-W., Rahman, R., Sytnikova, Y.A., Matts, J.A., Zeng, M., Gerlach, D., Yu, M., Berger, B., Naramura, M., Kile, B.T., et al. (2015). Conserved piRNA Expression from a Distinct Set of piRNA Cluster Loci in Eutherian Mammals. PLoS Genet. *11*, e1005652.

Claycomb, J.M., Batista, P.J., Pang, K.M., Gu, W., Vasale, J.J., van Wolfswinkel, J.C., Chaves, D.A., Shirayama, M., Mitani, S., Ketting, R.F., et al. (2009). The Argonaute CSR-1 and its 22G-RNA cofactors are required for holocentric chromosome segregation. Cell *139*, 123–134.

Daugherty, A.C., Yeo, R.W., Buenrostro, J.D., Greenleaf, W.J., Kundaje, A., and Brunet, A. (2017). Chromatin accessibility dynamics reveal novel functional enhancers in *C. elegans*. Genome Research *27*, 2096–2107.

Didion, J.P., Martin, M., and Collins, F.S. (2017). Atropos: specific, sensitive, and speedy trimming of sequencing reads. PeerJ *5*, e3720.

Drake, M., Furuta, T., Suen, K.M., Gonzalez, G., Liu, B., Kalia, A., Ladbury, J.E., Fire, A.Z., Skeath, J.B., and Arur, S. (2014). A Requirement for ERK-Dependent Dicer Phosphorylation in Coordinating Oocyte-to-Embryo Transition in C. elegans. Developmental Cell *31*, 614–628.

Esse, R., Gushchanskaia, E., Lord, A., and Grishok, A. (2018). DOT1L suppresses nuclear RNAi originating from enhancer elements in.

Evans, K.J., Huang, N., Stempor, P., Chesney, M.A., Down, T.A., and Ahringer, J. (2016). Stable *Caenorhabditis elegans* chromatin domains separate broadly expressed and developmentally regulated genes. Proceedings of the National Academy of Sciences *113*, E7020–E7029.

Gaydos, L.J., Rechtsteiner, A., Egelhofer, T.A., Carroll, C.R., and Strome, S. (2012). Antagonism between MES-4 and Polycomb Repressive Complex 2 Promotes Appropriate Gene Expression in C. elegans Germ Cells. Cell Reports *2*, 1169–1177.

Gaydos, L.J., Wang, W., and Strome, S. (2014). H3K27me and PRC2 transmit a memory of repression across generations and during development. Science *345*, 1515–1518.

Grishok, A. (2005). Transcriptional silencing of a transgene by RNAi in the soma of C. elegans. Genes & Development *19*, 683–696.

Gu, S.G., Pak, J., Guang, S., Maniar, J.M., Kennedy, S., and Fire, A. (2012). Amplification of siRNA in Caenorhabditis elegans generates a transgenerational sequence-targeted histone H3 lysine 9 methylation footprint. Nature Genetics *44*, 157–164.

Gu, W., Shirayama, M., Conte, D., Vasale, J., Batista, P.J., Claycomb, J.M., Moresco, J.J., Youngman, E.M., Keys, J., Stoltz, M.J., et al. (2009). Distinct Argonaute-Mediated 22G-RNA Pathways Direct Genome Surveillance in the C. elegans Germline. Molecular Cell *36*, 231–244.

Guang, S., Bochner, A.F., Pavelec, D.M., Burkhart, K.B., Harding, S., Lachowiec, J., and Kennedy, S. (2008). An Argonaute transports siRNAs from the cytoplasm to the nucleus. Science *321*, 537–541.

Guang, S., Bochner, A.F., Burkhart, K.B., Burton, N., Pavelec, D.M., and Kennedy, S. (2010). Small regulatory RNAs inhibit RNA polymerase II during the elongation phase of transcription. Nature *465*, 1097–1101.

Gullerova, M., and Proudfoot, N.J. (2012). Convergent transcription induces transcriptional gene silencing in fission yeast and mammalian cells. Nature Structural & Molecular Biology *19*, 1193–1201.

Han, T., Manoharan, A.P., Harkins, T.T., Bouffard, P., Fitzpatrick, C., Chu, D.S., Thierry-Mieg, D., Thierry-Mieg, J., and Kim, J.K. (2009). 26G endo-siRNAs regulate spermatogenic and zygotic gene expression in Caenorhabditis elegans. Proceedings of the National Academy of Sciences *106*, 18674–18679.

Holoch, D., and Moazed, D. (2015). RNA-mediated epigenetic regulation of gene expression. Nat. Rev. Genet. *16*, 71–84.

Huang, D.W., Sherman, B.T., Stephens, R., Baseler, M.W., Lane, H.C., and Lempicki, R.A. (2008). DAVID gene ID conversion tool. Bioinformation *2*, 428–430.

Iida, T., Nakayama, J., and Moazed, D. (2008). siRNA-Mediated Heterochromatin Establishment Requires HP1 and Is Associated with Antisense Transcription. Molecular Cell *31*, 178–189.

Langmead, B., Trapnell, C., Pop, M., and Salzberg, S.L. (2009). Ultrafast and memory-efficient alignment of short DNA sequences to the human genome. Genome Biology *10*, R25.

Lawrence, M., Huber, W., Pagès, H., Aboyoun, P., Carlson, M., Gentleman, R., Morgan, M.T., and Carey, V.J. (2013). Software for Computing and Annotating Genomic Ranges. PLoS Computational Biology *9*, e1003118.

Lee, H.-C., Gu, W., Shirayama, M., Youngman, E., Conte, D., and Mello, C.C. (2012). C. elegans piRNAs Mediate the Genome-wide Surveillance of Germline Transcripts. Cell *150*, 78–87.

Li, H. (2011). A statistical framework for SNP calling, mutation discovery, association mapping and population genetical parameter estimation from sequencing data. Bioinformatics *27*, 2987–2993.

Li, H., Handsaker, B., Wysoker, A., Fennell, T., Ruan, J., Homer, N., Marth, G., Abecasis, G., Durbin, R., and 1000 Genome Project Data Processing Subgroup (2009). The Sequence Alignment/Map format and SAMtools. Bioinformatics *25*, 2078–2079.

Li, W., Notani, D., and Rosenfeld, M.G. (2016). Enhancers as non-coding RNA transcription units: recent insights and future perspectives. Nature Reviews Genetics *17*, 207–223.

Liu, T., Rechtsteiner, A., Egelhofer, T.A., Vielle, A., Latorre, I., Cheung, M.-S., Ercan, S., Ikegami, K., Jensen, M., Kolasinska-Zwierz, P., et al. (2011). Broad chromosomal domains of histone modification patterns in C. elegans. Genome Research *21*, 227–236.

Luteijn, M.J., van Bergeijk, P., Kaaij, L.J.T., Almeida, M.V., Roovers, E.F., Berezikov, E., and Ketting, R.F. (2012). Extremely stable Piwi-induced gene silencing in Caenorhabditis elegans. EMBO J. *31*, 3422–3430.

Mao, H., Zhu, C., Zong, D., Weng, C., Yang, X., Huang, H., Liu, D., Feng, X., and Guang, S. (2015). The Nrde Pathway Mediates Small-RNA-Directed Histone H3 Lysine 27 Trimethylation in Caenorhabditis elegans. Current Biology *25*, 2398–2403.

Moazed, D., Buhler, M., Buker, S.M., Colmenares, S.U., Gerace, E.L., Gerber, S.A., Hong, E.-J.E., Motamedi, M.R., Verdel, A., Villen, J., et al. (2006). Studies on the Mechanism of RNAi-dependent Heterochromatin Assembly. Cold Spring Harbor Symposia on Quantitative Biology *71*, 461–471.

modENCODE Consortium, Celniker, S.E., Dillon, L.A.L., Gerstein, M.B., Gunsalus, K.C., Henikoff, S., Karpen, G.H., Kellis, M., Lai, E.C., Lieb, J.D., et al. (2009). Unlocking the secrets of the genome. Nature *459*, 927–930.

Ni, J., Chen, E., and Gu, S. (2014). Complex coding of endogenous siRNA, transcriptional silencing and H3K9 methylation on native targets of germline nuclear RNAi in C. elegans. BMC Genomics *15*, 1157.

Pefanis, E., Wang, J., Rothschild, G., Lim, J., Chao, J., Rabadan, R., Economides, A.N., and

Basu, U. (2014). Noncoding RNA transcription targets AID to divergently transcribed loci in B cells. Nature *514*, 389–393.

Pefanis, E., Wang, J., Rothschild, G., Lim, J., Kazadi, D., Sun, J., Federation, A., Chao, J., Elliott, O., Liu, Z.-P., et al. (2015). RNA Exosome-Regulated Long Non-Coding RNA Transcription Controls Super-Enhancer Activity. Cell *161*, 774–789.

Pikaard, C.S., and Mittelsten Scheid, O. (2014). Epigenetic Regulation in Plants. Cold Spring Harbor Perspectives in Biology *6*, a019315–a019315.

Quinlan, A.R. (2014). BEDTools: The Swiss-Army Tool for Genome Feature Analysis. Curr Protoc Bioinformatics *47*, 11.12.1-34.

Reich, D.P., Tyc, K.M., and Bass, B.L. (2018). *C. elegans* ADARs antagonize silencing of cellular dsRNAs by the antiviral RNAi pathway. Genes & Development *32*, 271–282.

Reinhart, B.J. (2002). Small RNAs Correspond to Centromere Heterochromatic Repeats. Science *297*, 1831–1831.

Riemondy, K.A., Sheridan, R.M., Gillen, A., Yu, Y., Bennett, C.G., and Hesselberth, J.R. (2017). valr: Reproducible genome interval analysis in R. F1000Res *6*, 1025.

Robinson, M.D., and Oshlack, A. (2010). A scaling normalization method for differential expression analysis of RNA-seq data. Genome Biology *11*, R25.

Robinson, M.D., McCarthy, D.J., and Smyth, G.K. (2010). edgeR: a Bioconductor package for differential expression analysis of digital gene expression data. Bioinformatics *26*, 139–140.

Sarkies, P., Ashe, A., Le Pen, J., McKie, M.A., and Miska, E.A. (2013). Competition between virus-derived and endogenous small RNAs regulates gene expression in Caenorhabditis elegans. Genome Research *23*, 1258–1270.

Schmitges, F.W., Prusty, A.B., Faty, M., Stützer, A., Lingaraju, G.M., Aiwazian, J., Sack, R., Hess, D., Li, L., Zhou, S., et al. (2011). Histone Methylation by PRC2 Is Inhibited by Active Chromatin Marks. Molecular Cell *42*, 330–341.

Seth, M., Shirayama, M., Gu, W., Ishidate, T., Conte, D., and Mello, C.C. (2013). The C. elegans CSR-1 argonaute pathway counteracts epigenetic silencing to promote germline gene expression. Dev. Cell *27*, 656–663.

Shen, E.-Z., Chen, H., Ozturk, A.R., Tu, S., Shirayama, M., Tang, W., Ding, Y.-H., Dai, S.-Y., Weng, Z., and Mello, C.C. (2018). Identification of piRNA Binding Sites Reveals the Argonaute Regulatory Landscape of the C. elegans Germline. Cell *172*, 937-951.e18.

Shirayama, M., Seth, M., Lee, H.-C., Gu, W., Ishidate, T., Conte, D., and Mello, C.C. (2012). piRNAs Initiate an Epigenetic Memory of Nonself RNA in the C. elegans Germline. Cell *150*, 65–77.

Speir, M.L., Zweig, A.S., Rosenbloom, K.R., Raney, B.J., Paten, B., Nejad, P., Lee, B.T., Learned, K., Karolchik, D., Hinrichs, A.S., et al. (2016). The UCSC Genome Browser database: 2016 update. Nucleic Acids Res. *44*, D717-725.

Stollar, V., and Stollar, B.D. (1970). Immunochemical Measurement of Double-stranded RNA of Uninfected and Arbovirus-Infected Mammalian Cells. Proceedings of the National Academy of Sciences *65*, 993–1000.

Sytnikova, Y.A., Rahman, R., Chirn, G.-W., Clark, J.P., and Lau, N.C. (2014). Transposable element dynamics and PIWI regulation impacts lncRNA and gene expression diversity in Drosophila ovarian cell cultures. Genome Res. *24*, 1977–1990.

Tabara, H., Yigit, E., Siomi, H., and Mello, C.C. (2002). The dsRNA binding protein RDE-4 interacts with RDE-1, DCR-1, and a DExH-box helicase to direct RNAi in C. elegans. Cell *109*, 861–871.

Tam, O.H., Aravin, A.A., Stein, P., Girard, A., Murchison, E.P., Cheloufi, S., Hodges, E., Anger, M., Sachidanandam, R., Schultz, R.M., et al. (2008). Pseudogene-derived small interfering RNAs regulate gene expression in mouse oocytes. Nature *453*, 534–538.

Tonkin, L.A. (2003). Mutations in RNAi Rescue Aberrant Chemotaxis of ADAR Mutants. Science *302*, 1725–1725.

Tsai, H.-Y., Chen, C.-C.G., Conte, D., Moresco, J.J., Chaves, D.A., Mitani, S., Yates, J.R., Tsai, M.-D., and Mello, C.C. (2015). A Ribonuclease Coordinates siRNA Amplification and mRNA Cleavage during RNAi. Cell *160*, 407–419.

Tyc, K.M., Nabih, A., Wu, M.Z., Wedeles, C.J., Sobotka, J.A., and Claycomb, J.M. (2017). The Conserved Intron Binding Protein EMB-4 Plays Differential Roles in Germline Small RNA Pathways of C. elegans. Developmental Cell *42*, 256-270.e6.

Vasale, J.J., Gu, W., Thivierge, C., Batista, P.J., Claycomb, J.M., Youngman, E.M., Duchaine, T.F., Mello, C.C., and Conte, D. (2010). Sequential rounds of RNA-dependent RNA transcription drive endogenous small-RNA biogenesis in the ERGO-1/Argonaute pathway. Proceedings of the National Academy of Sciences *107*, 3582–3587.

Venkatesh, S., Li, H., Gogol, M.M., and Workman, J.L. (2016). Selective suppression of antisense transcription by Set2-mediated H3K36 methylation. Nature Communications *7*, 13610.

Warf, M.B., Shepherd, B.A., Johnson, W.E., and Bass, B.L. (2012). Effects of ADARs on small RNA processing pathways in C. elegans. Genome Research *22*, 1488–1498.

Watanabe, T., Totoki, Y., Toyoda, A., Kaneda, M., Kuramochi-Miyagawa, S., Obata, Y., Chiba, H., Kohara, Y., Kono, T., Nakano, T., et al. (2008). Endogenous siRNAs from naturally formed dsRNAs regulate transcripts in mouse oocytes. Nature *453*, 539–543.

Wedeles, C.J., Wu, M.Z., and Claycomb, J.M. (2013). Protection of germline gene expression by the C. elegans Argonaute CSR-1. Dev. Cell *27*, 664–671.

Yigit, E., Batista, P.J., Bei, Y., Pang, K.M., Chen, C.-C.G., Tolia, N.H., Joshua-Tor, L., Mitani, S., Simard, M.J., and Mello, C.C. (2006). Analysis of the C. elegans Argonaute Family Reveals that Distinct Argonautes Act Sequentially during RNAi. Cell *127*, 747–757.

Yuan, W., Xu, M., Huang, C., Liu, N., Chen, S., and Zhu, B. (2011). H3K36 Methylation Antagonizes PRC2-mediated H3K27 Methylation. Journal of Biological Chemistry *286*, 7983–7989.

Zhang, Y., Liu, T., Meyer, C.A., Eeckhoute, J., Johnson, D.S., Bernstein, B.E., Nussbaum, C., Myers, R.M., Brown, M., Li, W., et al. (2008). Model-based Analysis of ChIP-Seq (MACS). Genome Biology *9*, R137.

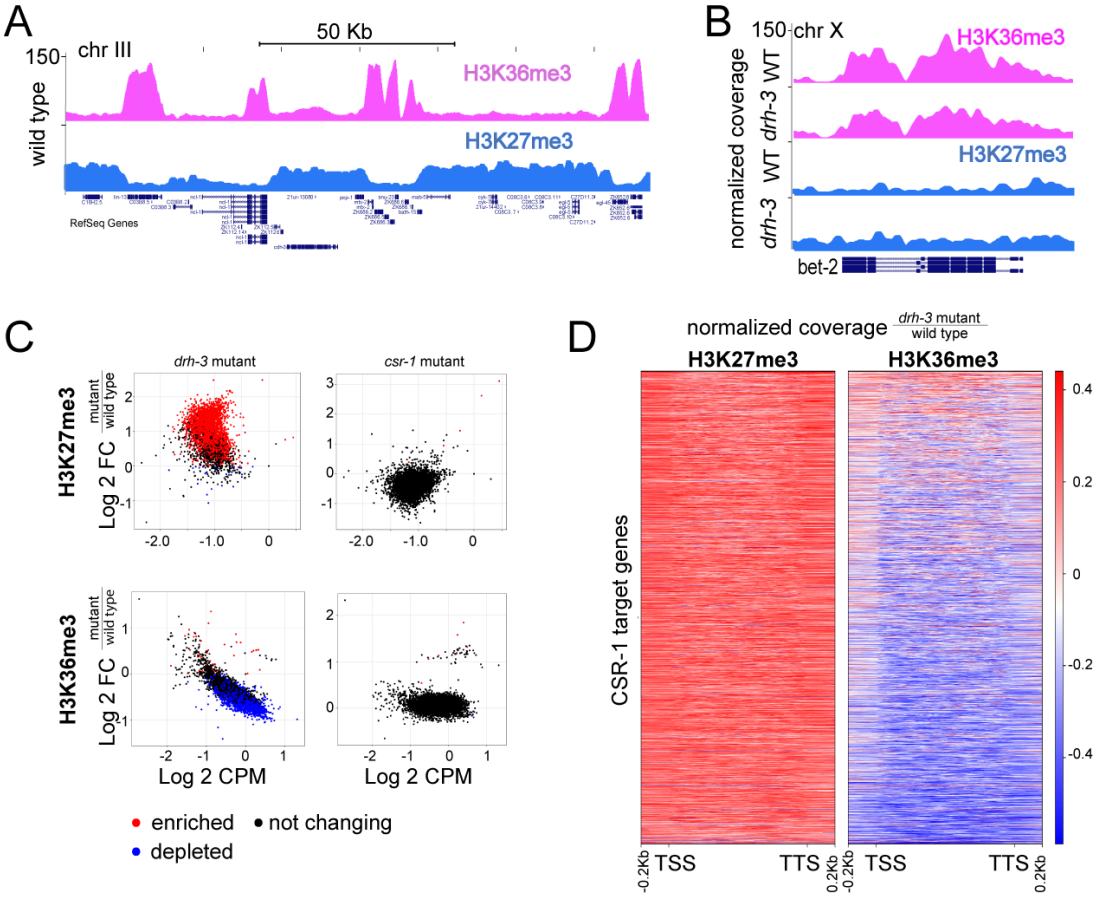

Figure 1. Ectopic H3K27me3 accumulation at highly expressed genes in *drh-3(ne4253)*. (A) Open chromatin is associated with H3K36me3 histone modification (pink), which opposes silencing histone mark H3K27me3 (blue). Highly expressed genes (CSR-1 targets: *ncl-1*, *lin-13*, *snu-23*) are enriched for H3K36me3 and depleted of H3K27me3. H3K27me3 is abundant at low expressed/silent regions. The peaks were generated with MACS2 peak calling algorithm (Galaxy version 2.0.10.2) (Zhang et al., 2008). (B) ChIP-seq normalized coverage for H3K36me3 (pink) and H3K27me3 (blue) demonstrating a decrease in H3K36me3, in *drh-3(ne4253)* mutant compared to wild type, and an increase in H3K27me3 modification at the highly expressed CSR-1 target gene *bet-2*. (C) Global increase in H3K27me3 and reduction of H3K36me3 at highly expressed CSR-1 target genes in *drh-3(ne4253)* mutant, but not in partially rescued *csr-1(tm892)* mutant. The normalization of both replicas was performed as described in Materials and Methods. The genome was divided into 50 bp bins and $\log_2$ fold change of bin coverage ratio between

mutant strain and wild type was calculated. Only the subclass of highly active genes (CSR-1 targets) is represented. The colors reflect the histone mark enrichment (red) and depletion (blue) observed in both biological replicates. (D) Heatmap demonstrating an increase in heterochromatic modification H3K27me3 and a decrease in activating modification H3K36me3 at actively transcribed gene coding regions in the *drh-3(ne4253)* mutant compared to wild type. The genome was divided into 50 bp bins and the ratio of normalized bin coverage between mutant and wild type was plotted on a heatmap. Each row corresponds to a CSR-1 target gene body between transcription start site (TSS) and transcription termination site (TTS) +/- 200 bp. Different gene length was approximated to be 1000 bp for the representation purpose. The mean value of 2 biological replicates was plotted.

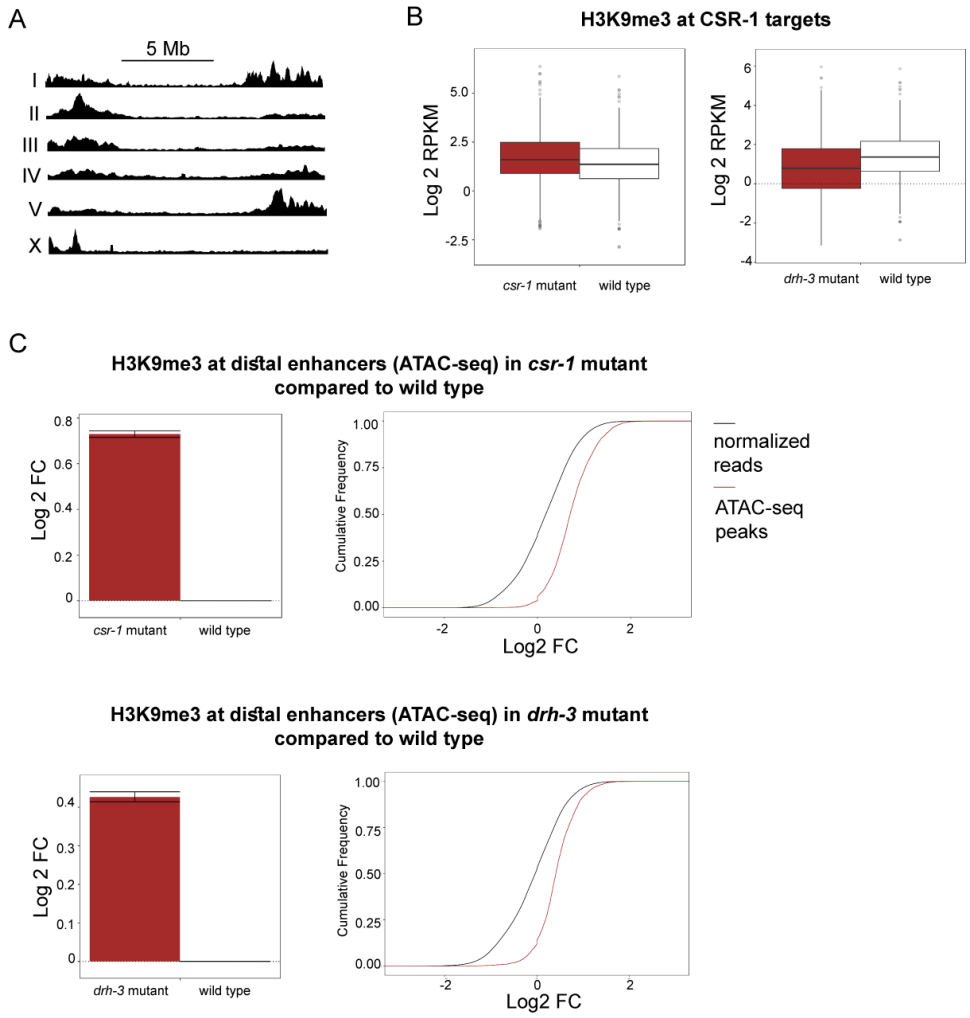

Figure 2. H3K9me3 alterations at actively transcribed genes and enhancers in partially rescued *csr-1(tm892)* and *drh-3(ne4253)*. (A) On the *C. elegans* autosomes, H3K9me3 is enriched at the chromosome arms and, on the X chromosome, only at the left arm. Read coverage in wild type worms (L3) normalized to, sequentially, RPKM and input is represented. (B) Box plot demonstrates an increase of H3K9 methylation at the CSR-1 target genes in *csr-1* mutant, but not in *drh-3 (ne4253)*. ChIP-seq data were normalized as described in methods. P-values<$2.2*10^{-16}$(Wilcoxon test) (C) Box plots and cumulative plots demonstrating H3K9me3 increase at distal (intergenic) enhancers detected by ATAC-seq (Daugherty et al., 2017) in *csr-1* and *drh-3* mutants compared to wild type. P-values<$2.2*10^{-16}$(Wilcoxon test).

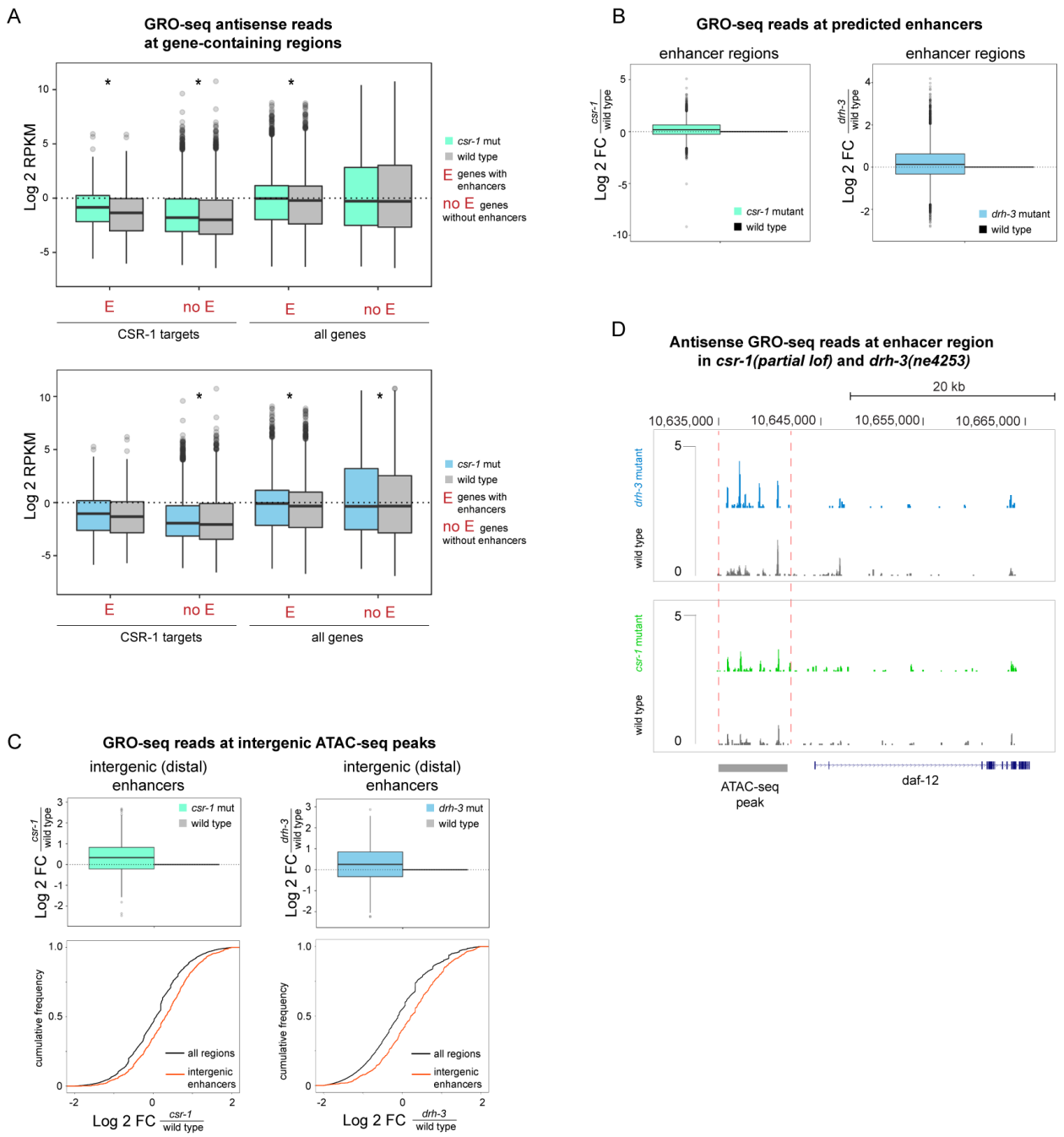

Figure 3. Elevated transcription at enhancer regions in partially rescued *csr-1(tm892)* and *drh-3(ne4253)*. (A) Box plots representing an increase in antisense GRO-seq read coverage (Cecere et al., 2014) at enhancer-containing genes and at CSR-1 targets with enhancers in *csr-1* (upper plot) and *drh-3* (lower plot) mutant L3 larva. *P-values <0.01 (Wilcoxon test). (B) Box plot demonstrating an increase in total GRO-seq read coverage at the putative enhancers (Evans

et al., 2016) in *csr-1* (left) or *drh-3* (right) mutant L3 larva. GRO-seq data (Cecere et al., 2014) were normalized as described in methods, and $\log_2$ transformed RPKM was plotted. P-values $<2.2*10^{-16}$ (Wilcoxon test). (C) GRO-seq read coverage is increased at distal enhancer regions (intergenic ATAC-seq peaks) in *csr-1* (left panel) and *drh-3* (right panel) mutants. *P-values <0.01 (Wilcoxon test). Analysis was performed as in (B). Cumulative plots confirming the GRO-seq data analysis for *csr-1* (on the left) and *drh-3* (on the right) mutants and demonstrating an increase in GRO-seq reads coverage in both mutants at distal enhancer regions (ATAC-seq data by (Daugherty et al., 2017)). (D) GRO-seq reads corresponding to antisense transcription are shown at the region containing a regulatory element detected by ATAC-seq upstream of the *daf-12* gene. An increase in the number of antisense reads is shown in *drh-3* (blue) and *csr-1* (green) mutants compared to wild type (grey).

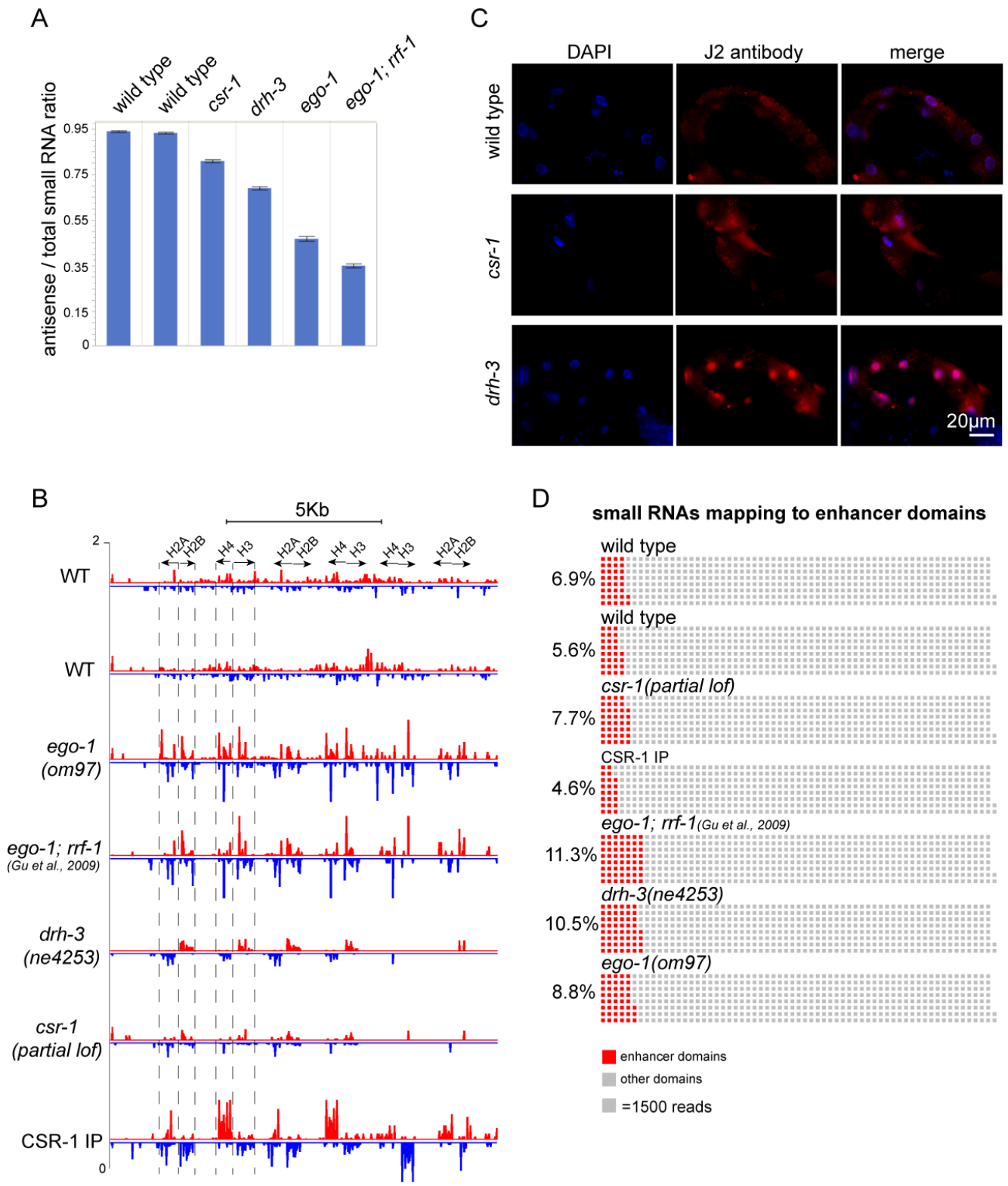
A
wild type
wild type
csr-1
drh-3
ego-1
ego-1; rrf-1
antisense / total small RNA ratio
0.95
0.75
0.55
0.35
0.15
0
C
DAPI
J2 antibody
merge
wild type
csr-1
drh-3
20μm
B
5Kb
H2A
H2B
H4
H3
WT
WT
ego-1
(om97)
ego-1; rrf-1
(Gu et al., 2009)
drh-3
(ne4253)
csr-1
(partial lof)
CSR-1 IP
2
0
D
small RNAs mapping to enhancer domains
wild type
6.9%
wild type
5.6%
csr-1(partial lof)
7.7%
CSR-1 IP
4.6%
ego-1; rrf-1(Gu et al., 2009)
11.3%
drh-3(ne4253)
10.5%
ego-1(om97)
8.8%
enhancer domains
other domains
=1500 reads

Figure 4. Changes in small RNA pools in the RdRP complex-mutants and partially rescued *csr-1(tm892)*.

(A) Decreased ratio of antisense/total small RNAs in RdRP mutants and *csr-1(lof)*. The small RNA data (Claycomb et al., 2009; Gu et al., 2009) were analyzed as described in Materials and Methods. The reads corresponding to miRNA and structure RNA were removed. Error bars represent 95% confidence interval. (B) Sense small RNAs and antisense small RNAs (depending on the directionality of gene transcription) are equally abundant in RdRP mutants and *csr-1(lof)*. A region on chromosome II containing a cluster of histone genes is shown. The reads on the positive strand are red, and those on the negative strand are blue. The bottom track represents the reads obtained by sequencing CSR-1-associated small RNAs that are antisense to the direction of gene transcription. The directionality of histone genes is marked with the arrows. (C) Images demonstrating an increase in nuclear dsRNA in *drh-3(ne4253)*. The worm intestines were extracted, fixed and stained with the J2 antibody. J2 foci preferentially accumulate in the intestine nuclei. Control worms were treated with RNase A to confirm the specificity of J2 antibody (Supplementary figure 2). D) Waffle plots representing small RNA presence at enhancer regions. Small RNA read coordinates were intersected with enhancer domain coordinates (Evans et al., 2016). Percentages of reads were obtained and grouped in blocks with each block representing 1500 reads. Small RNA reads mapped to enhancer regions are represented by red blocks and the percentage is shown on the left.

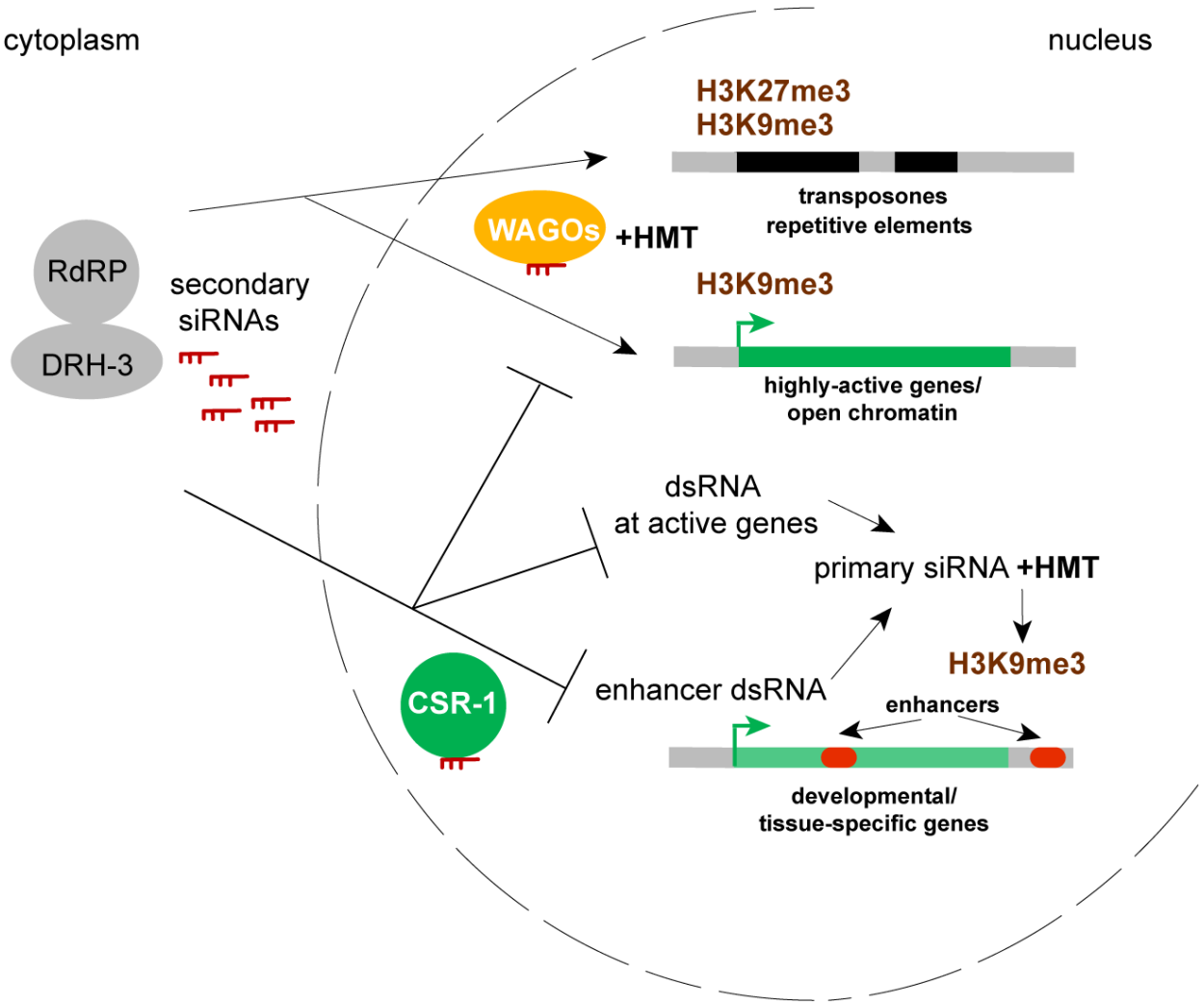

Figure 5. Model proposing that secondary (RdRP-produced) small RNAs prevent ectopic dsRNA formation and deposition of the silencing marks at enhancer elements and active genes in *C. elegans.*

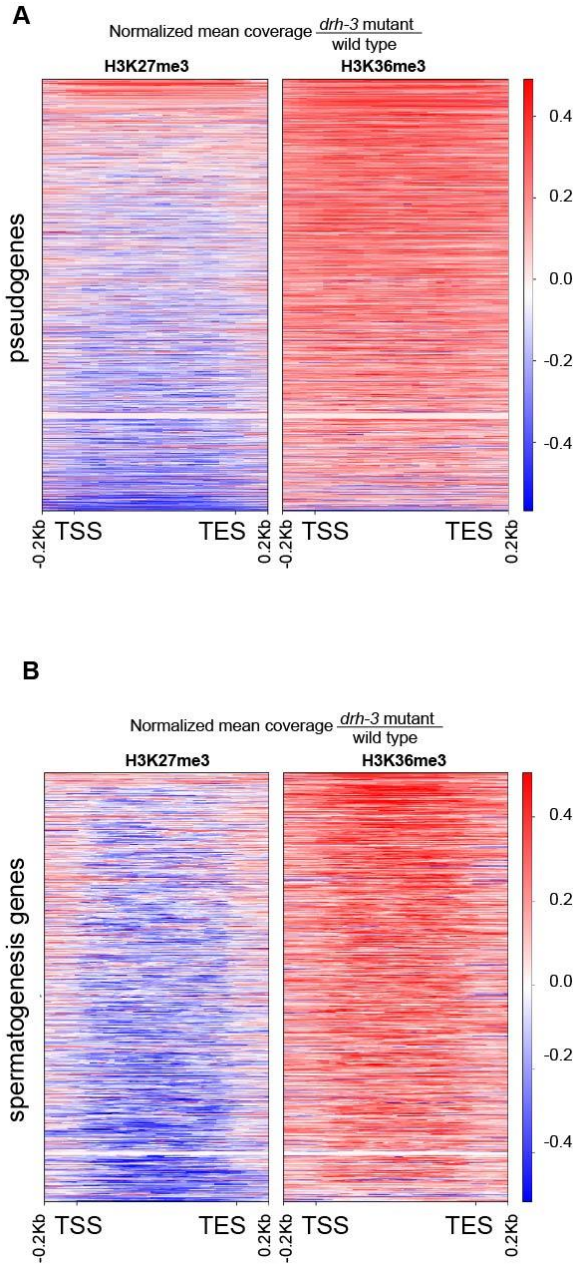

Supplementary figure 1, related to Figure 1. Loss of H3K27me3 at the pseudogenes and tissue-specific genes (spermatogenesis) genes in drh-3(ne4253). (A) Heatmap demonstrating a decrease in silencing modification H3K27me3 and an increase in activating modification H3K36me3 at pseudogenes in *drh-3(ne4253)* compared to wild type. The genome was divided into 50 bp bins and the ratio of normalized bin coverage between mutant and wild type was plotted on a heatmap. Each row corresponds to pseudogene coding regions between transcription start site (TSS) and transcription termination site (TTS) +/- 200 bp. Different gene length was approximated to be 1000 bp for the representation purpose. The mean value of 2 biological replicates is shown. (B) same as on (A) for tissue-specific genes represented by spermatogenesis genes.

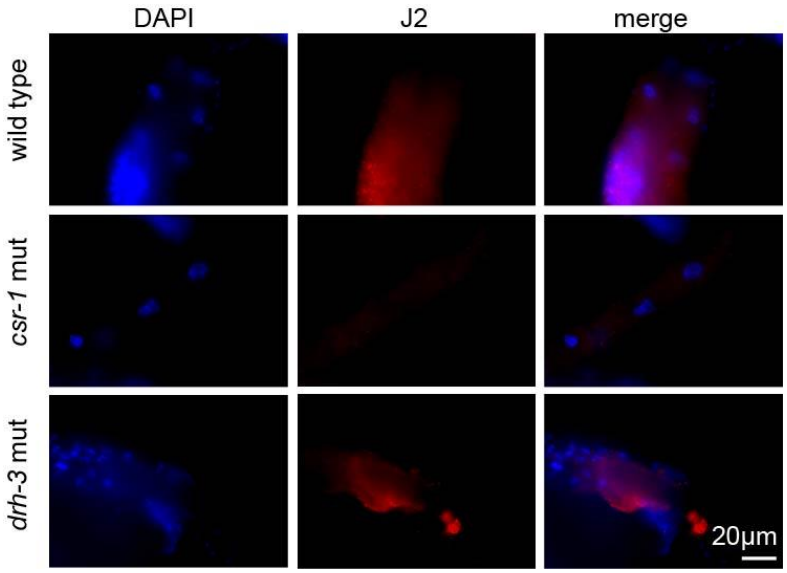

Supplementary figure 2, related to Figure 4. Images demonstrating the absence of J2 foci after treatment with RNAse A.

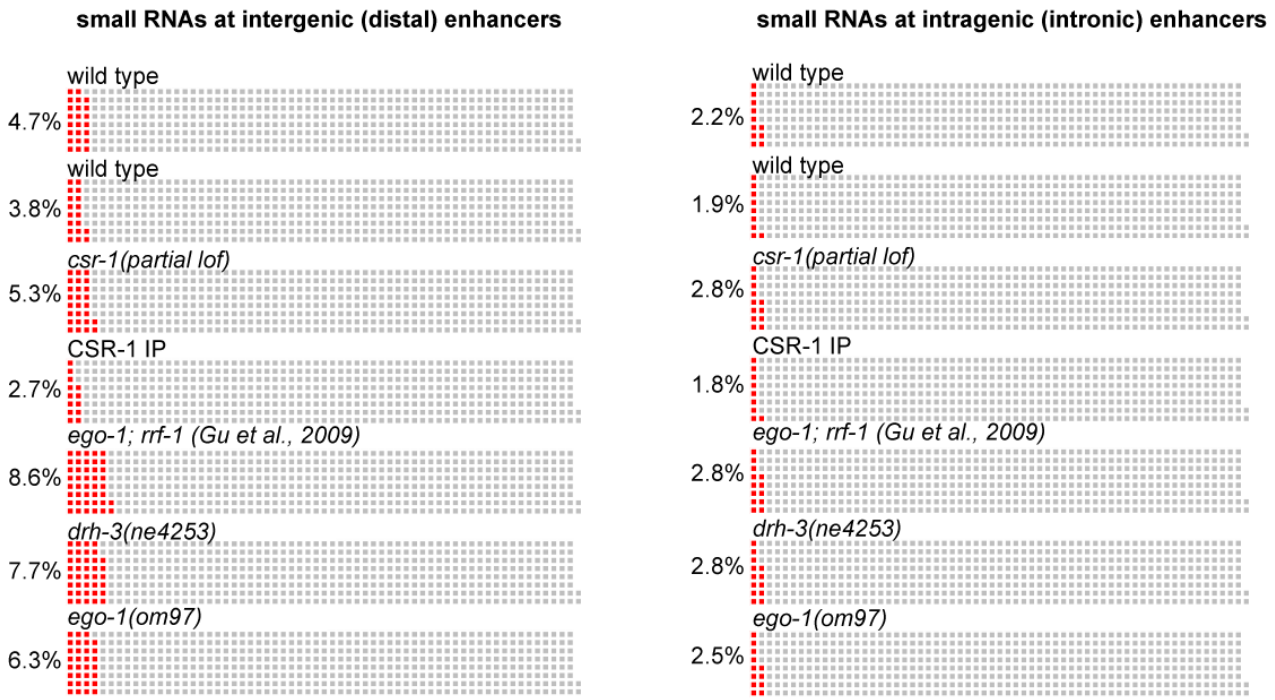

Supplementary figure 3, related to Figure 4. Small RNAs map to putative enhancer regions. Waffle plots representing small RNA presence at intergenic and intragenic enhancer regions. Small RNA read coordinates were intersected with enhancer domain coordinates (Evans et al., 2016). Percentages of reads were obtained and grouped in blocks with each block representing 1500 reads. Small RNA reads mapped to enhancer regions are represented by red blocks and the percentage is shown on the left.

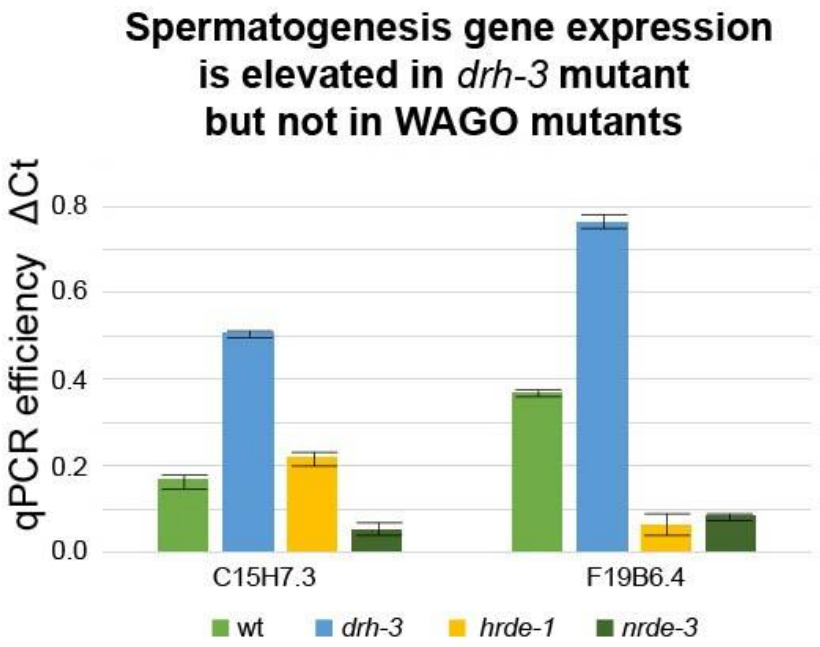

Supplementary figure 4, related to Figure 1. Expression of spermatogenesis genes is increased in *drh-3*, but not in *hrde-1* and *nrde-3* mutants. Expression of two spermatogenesis genes was detected by real-time PCR following reverse transcription. qPCR was normalized to the housekeeping gene *csq-1*. Primers: C15H7.3 (forward GAATGGTCCGGAGAGTTTCA, reverse AGCTATGCTCTCCTGGTGGA); F19B6.4 (forward AACCCTCACAGTCCGAGAGA, reverse GTCATGGTTCCGACTTTCGT); *csq-1*(forward GGCATCTCCAAAAACGAAGA, reverse ACCGATTTGGTGTCTTCAGC).

Supplemental Table 1. Total number of reads and reads mapped to the genome.

	H3K9me3		H3K27me3		H3K36me3		input	
	total	mapped	total	mapped	total	mapped	total	mapped
csr-1 mut rep 1	23465228	17324774	17264566	14309101	24209314	21975075	24174007	21250392
csr-1 mut rep 2	19230095	15320436	23299511	19572782	23613175	21385887	25758059	22658240
drh-3 mut rep 1	21295730	16914110	25327471	21393150	22454777	19623892	28210827	24297709
drh-3 mut rep 2	21953531	17507601	27317317	22749977	24748460	21733122	30933546	25947358
wild type rep 1	29553987	23069163	22723459	19110788	19689267	18077502	22820660	19952313
wild type rep 2	20252239	16729488	24840857	20216133	27644022	25013183	32142113	28179397

Supplemental Table 2. Pearson correlation coefficients.

Experiment	Pearson correlation coefficient
N2_input_rep_1 x N2_input_rep_2	0.99
*csr-1*_input_rep_1 x *csr-1*_input_rep_2	0.99
*drh-3*_input_rep_1 x *drh-3*_input_rep_2	0.96
N2_H3K9me3_rep_1 x N2_H3K9me3_rep_2	0.68
*csr-1*_H3K9me3_rep_1 x *csr-1*_H3K9me3_rep_2	0.7
*drh-3*_H3K9me3_rep_1 x *drh-3*_H3K9me3_rep_2	0.94
N2_H3K27me3_rep_1 x N2_H3K27me3_rep_2	0.96
*csr-1*_H3K27me3_rep_1 x *csr-1*_H3K27me3_rep_2	0.91
*drh-3*_H3K27me3_rep_1 x *drh-3*_H3K27me3_rep_2	0.68
N2_H3K36me3_rep_1 x N2_H3K36me3_rep_2	0.97
*csr-1*_H3K36me3_rep_1 x *csr-1*_H3K36me3_rep_2	0.88
*drh-3*_H3K36me3_rep_1 x *drh-3*_H3K36me3_rep_2	0.97

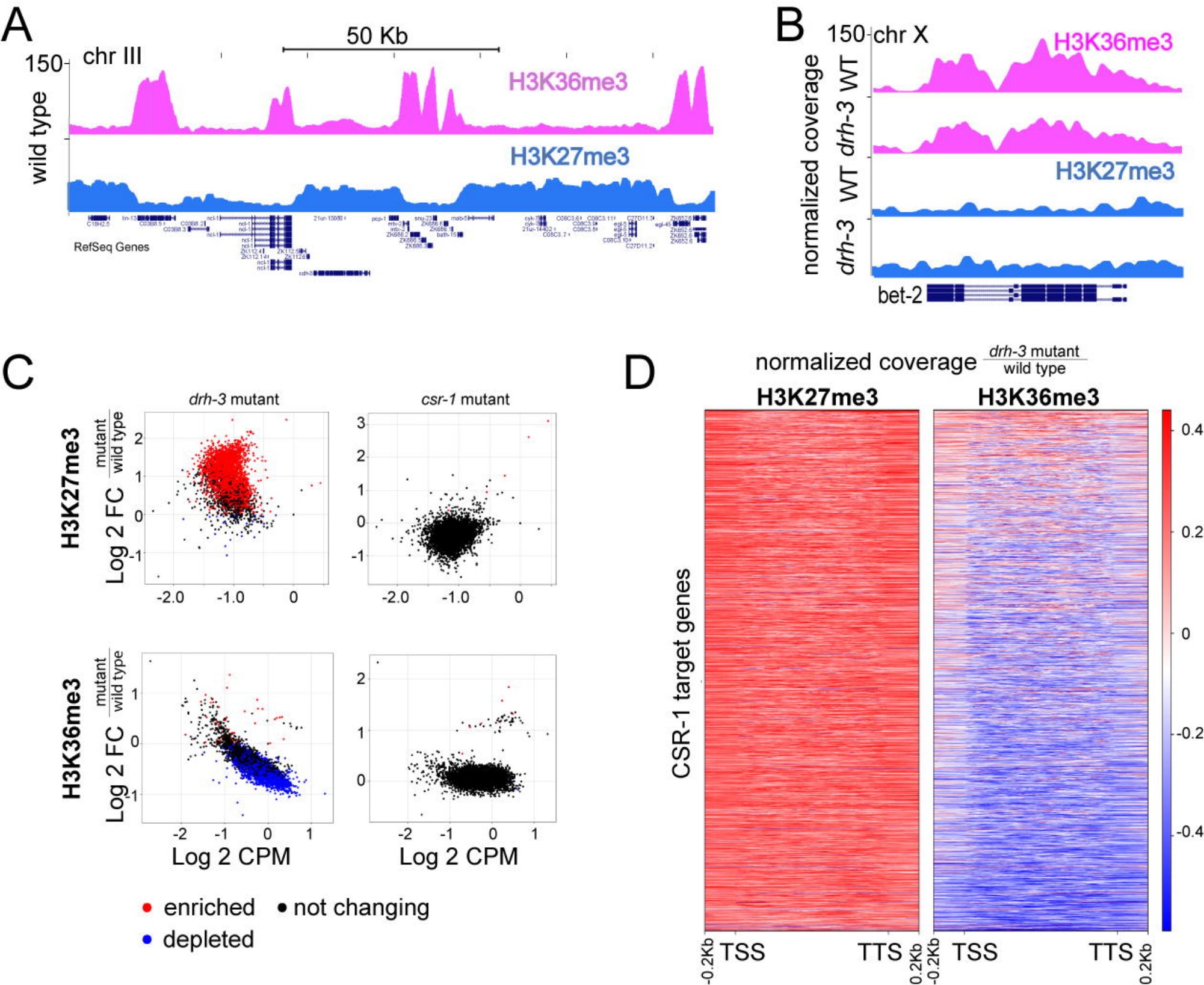
A
50 Kb
150
chr III
wild type
H3K36me3
H3K27me3
RefSeq Genes
B
150
chr X
H3K36me3
normalized coverage
WT
drh-3
WT
drh-3
H3K27me3
bet-2
C
drh-3 mutant
csr-1 mutant
H3K27me3
H3K36me3
mutant / wild type
Log 2 FC
Log 2 CPM
enriched
not changing
depleted
D
normalized coverage drh-3 mutant / wild type
H3K27me3
H3K36me3
CSR-1 target genes
-0.2Kb
TSS
TTS
0.2Kb
0.4
0.2
0
-0.2
-0.4

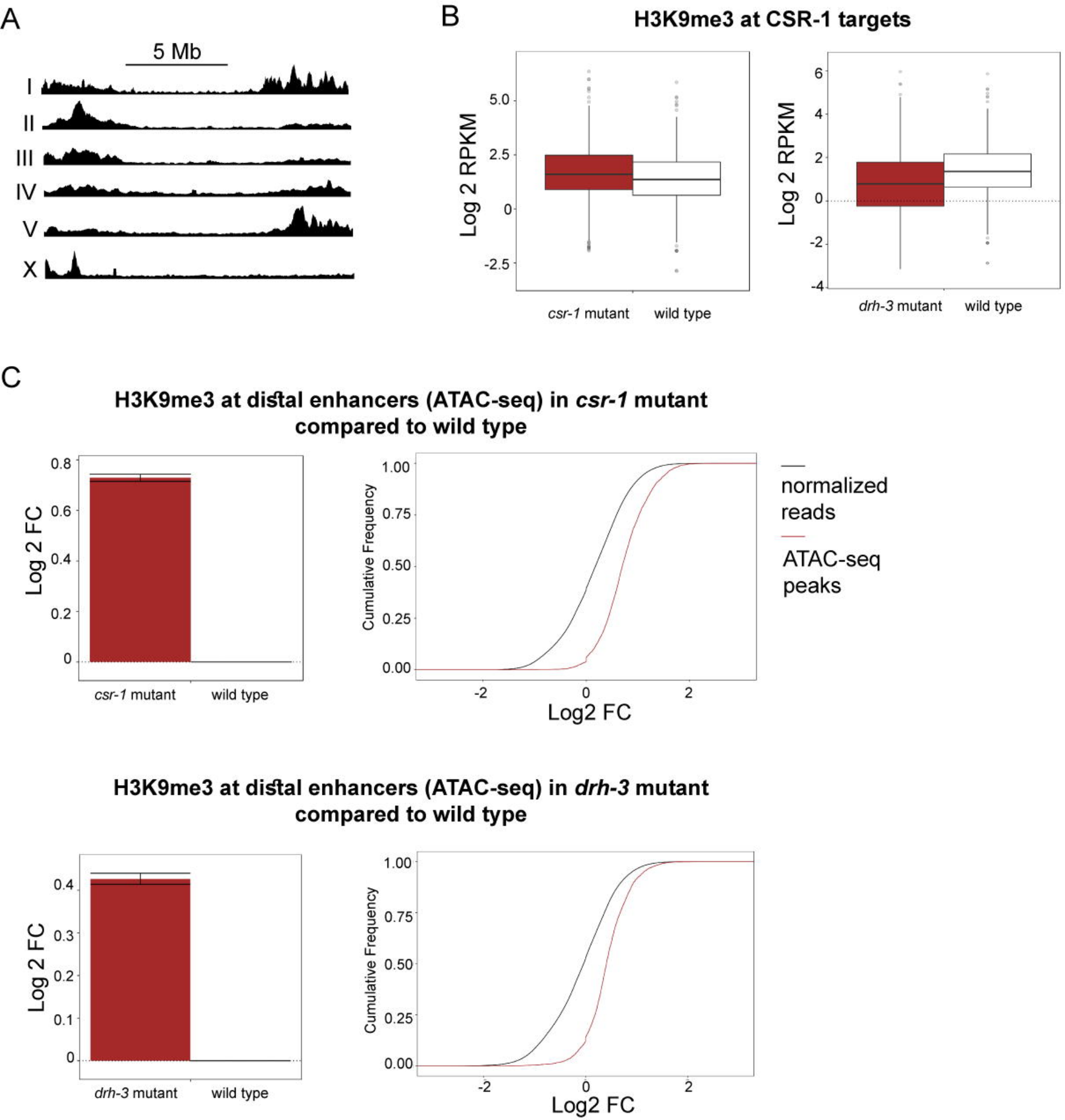
A
5 Mb
I
II
III
IV
V
X
B
H3K9me3 at CSR-1 targets
Log 2 RPKM
5.0
2.5
0
-2.5
csr-1 mutant
wild type
Log 2 RPKM
6
4
2
0
-2
-4
drh-3 mutant
wild type
C
H3K9me3 at distal enhancers (ATAC-seq) in csr-1 mutant compared to wild type
Log 2 FC
0.8
0.6
0.4
0.2
0
csr-1 mutant
wild type
Cumulative Frequency
1.00
0.75
0.50
0.25
0.00
-2
0
2
Log2 FC
normalized reads
ATAC-seq peaks
H3K9me3 at distal enhancers (ATAC-seq) in drh-3 mutant compared to wild type
Log 2 FC
0.4
0.3
0.2
0.1
0
drh-3 mutant
wild type
Cumulative Frequency
1.00
0.75
0.50
0.25
0.00
-2
0
2
Log2 FC

A

GRO-seq antisense reads at gene-containing regions

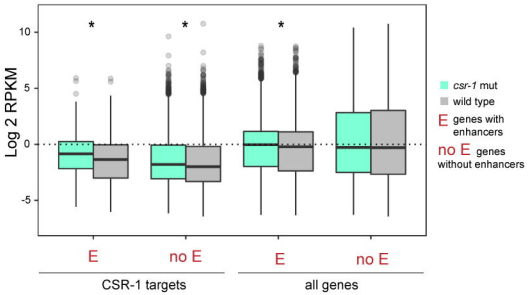

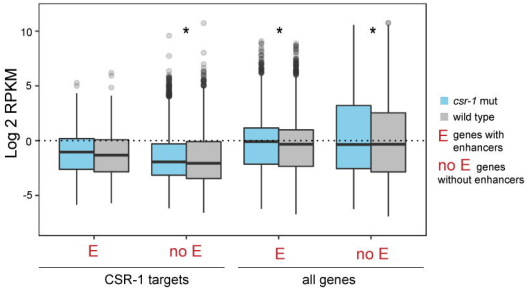

B

GRO-seq reads at predicted enhancers

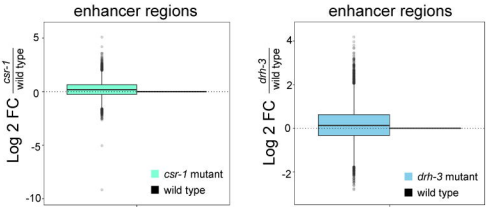

C

GRO-seq reads at intergenic ATAC-seq peaks

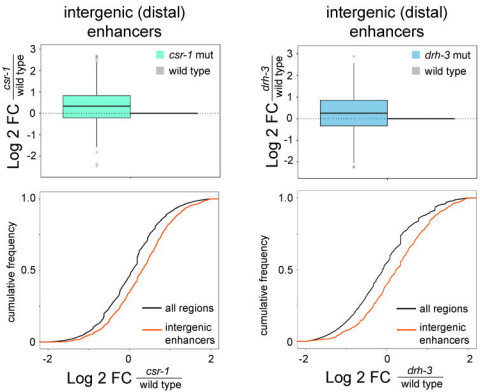

D

Antisense GRO-seq reads at enhacer region in *csr-1(partial lof)* and *drh-3(ne4253)*

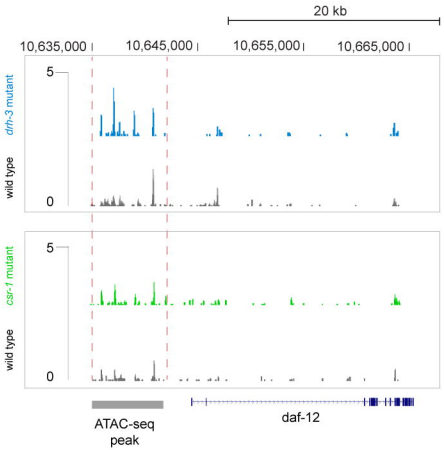

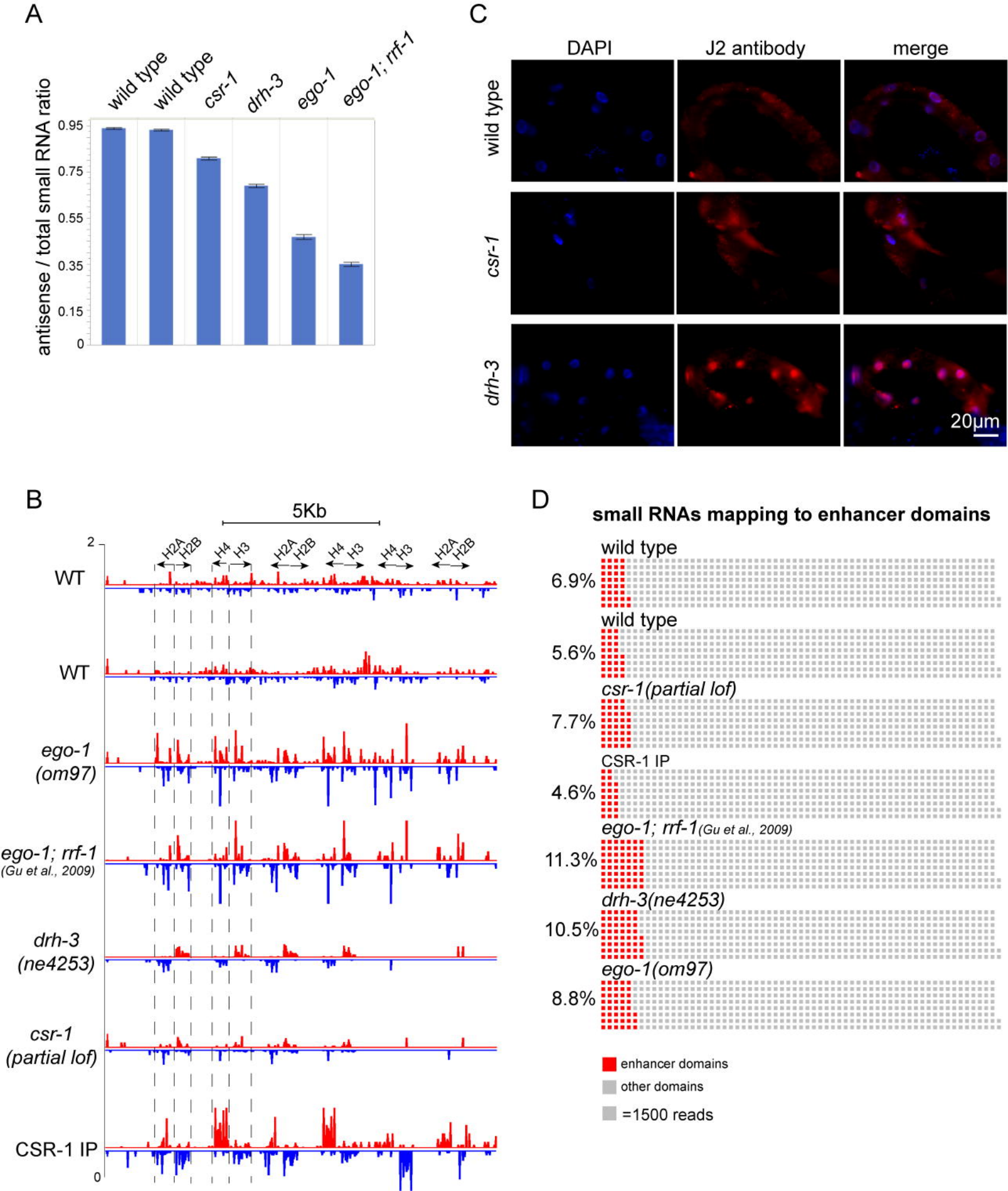
A
wild type
wild type
csr-1
drh-3
ego-1
ego-1; rrf-1
antisense / total small RNA ratio
0.95
0.75
0.55
0.35
0.15
0
C
DAPI
J2 antibody
merge
wild type
csr-1
drh-3
20μm
B
5Kb
H2A
H2B
H4
H3
WT
WT
ego-1
(om97)
ego-1; rrf-1
(Gu et al., 2009)
drh-3
(ne4253)
csr-1
(partial lof)
CSR-1 IP
2
0
D
small RNAs mapping to enhancer domains
wild type
6.9%
wild type
5.6%
csr-1(partial lof)
7.7%
CSR-1 IP
4.6%
ego-1; rrf-1(Gu et al., 2009)
11.3%
drh-3(ne4253)
10.5%
ego-1(om97)
8.8%
enhancer domains
other domains
=1500 reads

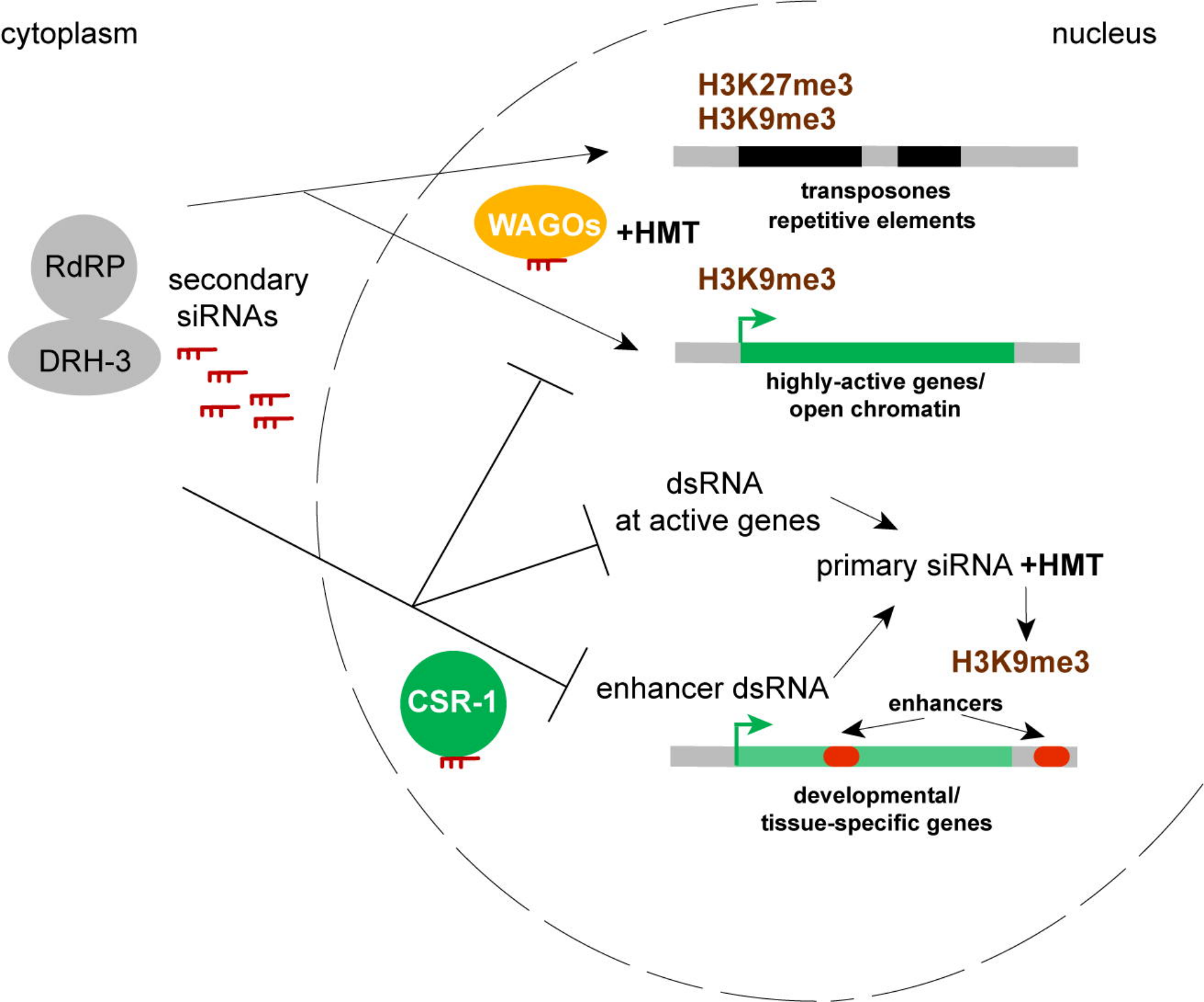
cytoplasm
nucleus
H3K27me3
H3K9me3
transposones
repetitive elements
WAGOs
+HMT
RdRP
DRH-3
secondary
siRNAs
H3K9me3
highly-active genes/
open chromatin
dsRNA
at active genes
primary siRNA +HMT
H3K9me3
enhancer dsRNA
enhancers
CSR-1
developmental/
tissue-specific genes